Dynamic evolution of competing same-dip double subduction: New perspectives of the Neo-Tethyan plate tectonics

Arnab Roy[1], Nibir Mandal[1], Jeroen Van Hunen[2]

[1]Department of Geological Sciences, Jadavpur University Kolkata
700032, India.
[2]2Department of Earth Sciences, Durham University, Durham, UK

This manuscript has been submitted for publication in Earth and Planetary Science Letters. Please note that the manuscript has not undergone any peer-review process. Subsequent versions of this manuscript may have slightly different content. If accepted, the final version of this manuscript will be available via a link on this webpage. Please feel free to contact any of the authors if you have questions or feedback.

Abstract

Same-dip double-subduction (SDDS) systems are widely reported from present as well as past complex convergent plate tectonic configurations. However, the dynamics of their evolution is poorly understood, which is crucial to conceptualize anomalous subducting slab kinematics and associated observed geological phenomena, such as irregular trench migration rates, high convergence velocities, and slab break-off. To bridge this gap, we develop dynamic thermo-mechanical subduction models and investigate the initiation and evolution of SDDS systems, considering three different initial plate configurations: oceanic, oceanic-continental and multiple continental settings, based on Neo-Tethyan paleo-reconstructions. Each model offers new insights into the complex tectonic history of the major Neo-Tethyan subduction zones, particularly the Indo-Eurasian and Andaman convergent systems. We evaluate the slab-slab interactions, trench and subduction kinematics, inter-plate reorganization, and temporally varying mantle flow patterns involved in the dynamic evolution of these SDDS systems. The oceanic SDDS model simulations reveal that a sizable oceanic plate can initiate two subduction zones synchronously, but will evolve unequally in a competing mode, leading to exceptionally high convergence rates (~16-17 cm/year) for a prolonged duration (~7-8 Myr). This finding explains the coeval activity of coupled subduction zones in the Indo-Eurasia convergence during the Cretaceous evolution of the Neo-Tethys. The ocean-continent SDDS model, on the other hand, localizes subduction preferentially at passive margins between the oceanic plate and the continental block, forming double subduction zones that grow almost equally to form a spreading centre between the two trenches. These model results allow us to reconstruct the Cenozoic evolution of the eastern Neo-Tethyan region, which ultimately led to the development of the Andaman subduction zone. We also show the post-Cretaceous evolution of the Indo-Eurasian collision zone as a consequence of the SDDS dynamics in presence of multiple continental blocks. These dynamics facilitated slab break-off, transforming the SDDS into a single subduction system in a relatively short time frame (~3 Myr). We finish with a synthesis of the paleo-reconstructions of the Neo-Tethys in the perspective of these SDDS models.

Keywords: Convergent plate tectonics, double subduction systems, dynamic subduction modelling, Finite element method, slab interaction, spreading centre locations, tectonic evolution of Neo-Tethys

1. Introduction

Subduction zones are spectacular planetary-scale manifestations of the convergent plate tectonics, and they govern a wide range of geological phenomena, such as continental crust formation, magmatism and geochemical recycling, and geophysical processes, such as earthquake localization and energy dissipation. Consequently, understanding their geodynamics has become a major concern in plate tectonic studies, especially to interpret terrestrial seismic and volcanic hazards that greatly influence the Earth's climate and environment (Corbi et al., 2017; Stern, 2002; Tilling, 1996). Subduction tectonics often turn complicated due to complex configurations of multiple plates, kinematically linked with one another. Double subduction systems are a common example of such convergent settings, where two lithospheric slabs subduct synchronously along sub-parallel trenches (Fig. 1). They are widely reported from the present-day plate configurations

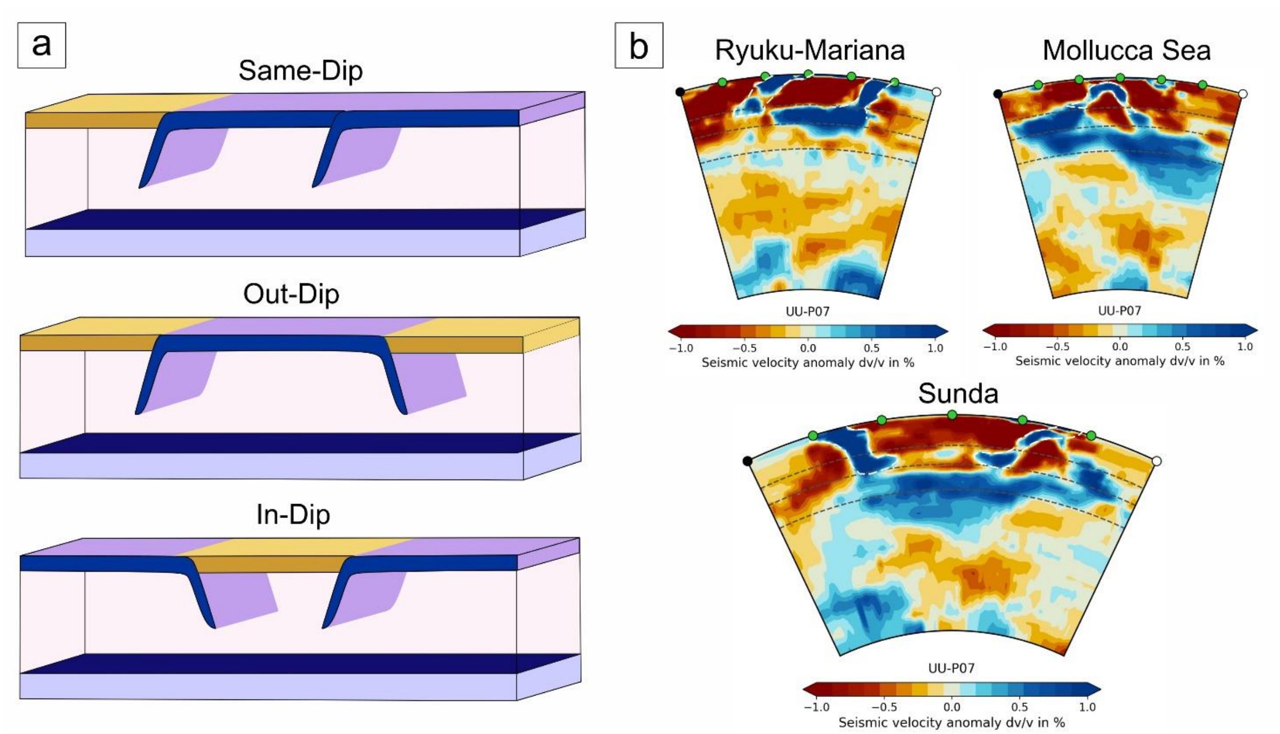

Figure 1: Illustrations showing a) the three different types of double subduction systems and b) their natural counterparts observed from seismic tomography. The P-wave models which are used for this analysis are GAP-P4, and UU-P07 (Fukao & Obayashi, 2013; Obayashi et al. 2013; Amaru, 2007)

(Fig. 1), e.g., the Mediterranean (Király et al., 2018; Vignaroli et al., 2008), the Molucca Sea (Zhang et al., 2017), Taiwan (Lin and Kuo, 2016), New Zealand (Lamb, 2015), and around the Philippines plate (Ryukyu vs. Izu-Bonin-Mariana trenches; (Faccenna et al., 2018; Hall and Spakman, 2002)), as well as from paleo-reconstructions, e.g., Trans-Tethyan System (Jagoutz et al., 2015), Indian Block and Eastern Cathaysia Block configuration of supercontinent Columbia (Phukon, 2022), Late Cretaceous eastern Turkey evolution (Eyuboglu et al., 2019). The double-subduction model has recently received much attention to address the problem of enigmatic slab kinematics encountered at both modern and ancient convergent zones (Čížková and Bina, 2015; Dasgupta and Mandal, 2018; Jagoutz et al., 2015). Based on seismic tomography and available plate kinematics data from GPS observations, three types of double-subduction configurations (Király et al., 2021) have been recognized: outward-, inward- and same-dipping slabs (Fig. 1). Despite significant research advancements on the first two types, the dynamics of same-dip double subduction has remained poorly understood, which is the principal concern to address in the present article with a focus upon the Neo-Tethyan tectonic evolution.

Plate reconstruction studies suggest that same-dip double subduction (SDDS) systems developed repeatedly in the course of the Neo-Tethyan evolution covering a long time span of ~150 Myr (Hall, 2012; Kufner et al., 2016; Pusok and Stegman, 2020). Using quantitative models, Jagoutz et al. (2015) have shown the existence of coupled subduction zones in the Trans-Tethyan intra-oceanic system below the southern margin of Eurasia. During the Cretaceous to Early Tertiary period, this tectonic system evolved through multiple Neo-Tethyan subduction episodes, featuring the Kshiroda Plate's north-dipping oceanic slab under Eurasia (Yin and Harrison, 2000) and intra-oceanic subduction of the northern oceanic segment of the Indian subcontinent beneath the Kshiroda Plate. Geological, geochemical, and paleomagnetic investigations into the tectonic units, specifically the forearc, oceanic melange, and ophiolite sequences within the Himalayas (Aitchison et al., 2000; Bouilhol et al., 2013; Hall, 2012; Yin and Harrison, 2000) imply the existence of concurrent subduction of two parallel slabs with similar dipping orientations. Complementing these findings, geophysical observations, such as the detection of multiple slab remnants through seismic tomography models (Van Der Voo et al., 1999), and alterations in trench kinematics and the upper plate's deformation patterns (Gürer et al., 2016; Jolivet et al., 2018), further reinforce the argument in favour of SDDS. Similarly, recent works have recognized multiple interacting double-subduction events to reconstruct the evolution of the Andaman Subduction system (Advokaat et al., 2018; Bandyopadhyay et al., 2020; Ghosh et al., 2017). The active tectonics in Andaman occurs at the northern flank of the Java trench where the oceanic part of the Indian Plate subducts at a low angle to the arc-trend beneath the Andaman microcontinental block as the overriding plate. Geochronological correlations and geochemical signatures of the arc volcanism (Westerweel et al., 2019) and ophiolitic suites (Acharyya et al., 1991) indicate the activity of a second subduction zone on the eastern side at the time of late-Miocene subduction (continuing to present day). In addition, geochemical evidence (Ghosh et al. 2017) suggests that the morphology of the Andaman-Nicobar outer-arc high grew from the coalescence of two accretionary prisms linked to the double-subduction tectonics. Despite a significant advancement in terms of various geochemical and geophysical information, dynamically self-consistent geodynamic models that can comprehensively integrate various geological processes of these SDDS systems were left unexplored.

Recent analogue and numerical modelling have dealt with the complexities in double-subduction evolution and their effects on the regional plate motion, intraplate deformations, slab interactions and topographic developments (Dasgupta and Mandal, 2018; Holt et al., 2017; Király et al., 2021; Mishin et al., 2008; Peral et al., 2018; Pusok and Stegman, 2019). It is now a well-established fact that their mode of development largely differs from that of a single-subduction system. The additional complexity originates primarily from inter-slab interactions that greatly influence the plate bending and viscous dissipation in the mantle, coupled with additional factors, such as contrasting plate ages, plate dimensions, rheology, and inter-slab distance (Čížková and Bina, 2015; Dasgupta and Mandal, 2018; Holt et al., 2017). The initial relative arrangement of tectonic plates is another influential factor considered in the double-subduction evolution. For instance, the Ryukyu-IBM system has an intra-oceanic subduction zone coupled with another subduction zone at an ocean-continent convergence boundary. In contrast, the Trans-Tethyan double subduction formed with the Indian continental plate linked to the subducting oceanic counterpart. This difference in the initial plate arrangements might have led to their contrasting evolutionary paths, resulting in a completely different tectonic history of these two regions. However, how the initial plate tectonic configuration governs the dynamic evolution of a SDDS system is still an open-ended question, which the present article addresses in the context of the Neo-Tethyan subduction tectonics. This investigation additionally accounts for the effects of crucial processes that commonly influence the subduction dynamics, e.g., trench and subduction kinematics, inter-plate reorganization, and onset of slab break-off.

We develop geodynamic models to simulate the thermo-mechanical evolution of SDDS systems, initiated along pre-existing lithospheric weaknesses and reconstruct the evolutionary history of both the Indo-Eurasian and Andaman double subduction systems, as discussed above. The models are designed to simulate time-dependent and self-consistently evolving subduction for a given plate configuration. This modelling allows to address the following key questions: 1) can two adjacent subduction zones with the same dip angle grow concurrently, and 2) if they can, how do these neighbouring subduction zones mutually influence each other during their evolution, depending on their initial tectonic configurations? We also explore the following influential phenomena: a) mutual interactions of simultaneously operating subducting slab motion during the evolution of commonly reported Neo-Tethyan SDDS systems, b) complexity in the associated mantle flow patterns and their role in localization of lithospheric-scale extensional zones in convergent tectonics, and c) slab detachment leading to a transition from double to single subduction process.

2. Numerical Modelling Approach

2.1.Model Design

We use 2D thermomechanical numerical models (Fig. 2) that are inherently dynamic, implying that no external forces or velocities are applied to the overall system. Details of the numerical method are provided in Appendix A. The model domain represents a vertical rectangular section, covering a depth of 1000 km and a horizontal distance of 7000 km (Fig. 2a). The upper and lower model boundaries are subjected to a free-slip (zero shear stress) condition, and the two sidewalls are assigned a periodic condition. We introduce mechanical weaknesses in the lithospheric layer, as considered in previous studies that suggested spontaneous subduction initiation to occur preferentially at the locations of pre-existing lithospheric weakness, e.g., transform faults (Arcay et al., 2020; Zhou et al., 2018). This weak-zone perturbation model of subduction initiation is a viable mechanical model in the light of damage theory proposed by Bercovici & Ricard, 2014. The lithospheric weakness is represented as a narrow (10 km wide), low-viscosity (10^{20} Pa s) zone, extending to the lithospheric base (Fig. 2). The weak zones can also characterize intraplate lithosphere-scale faults that develops in large oceanic plates, similar to the present-day Wharton

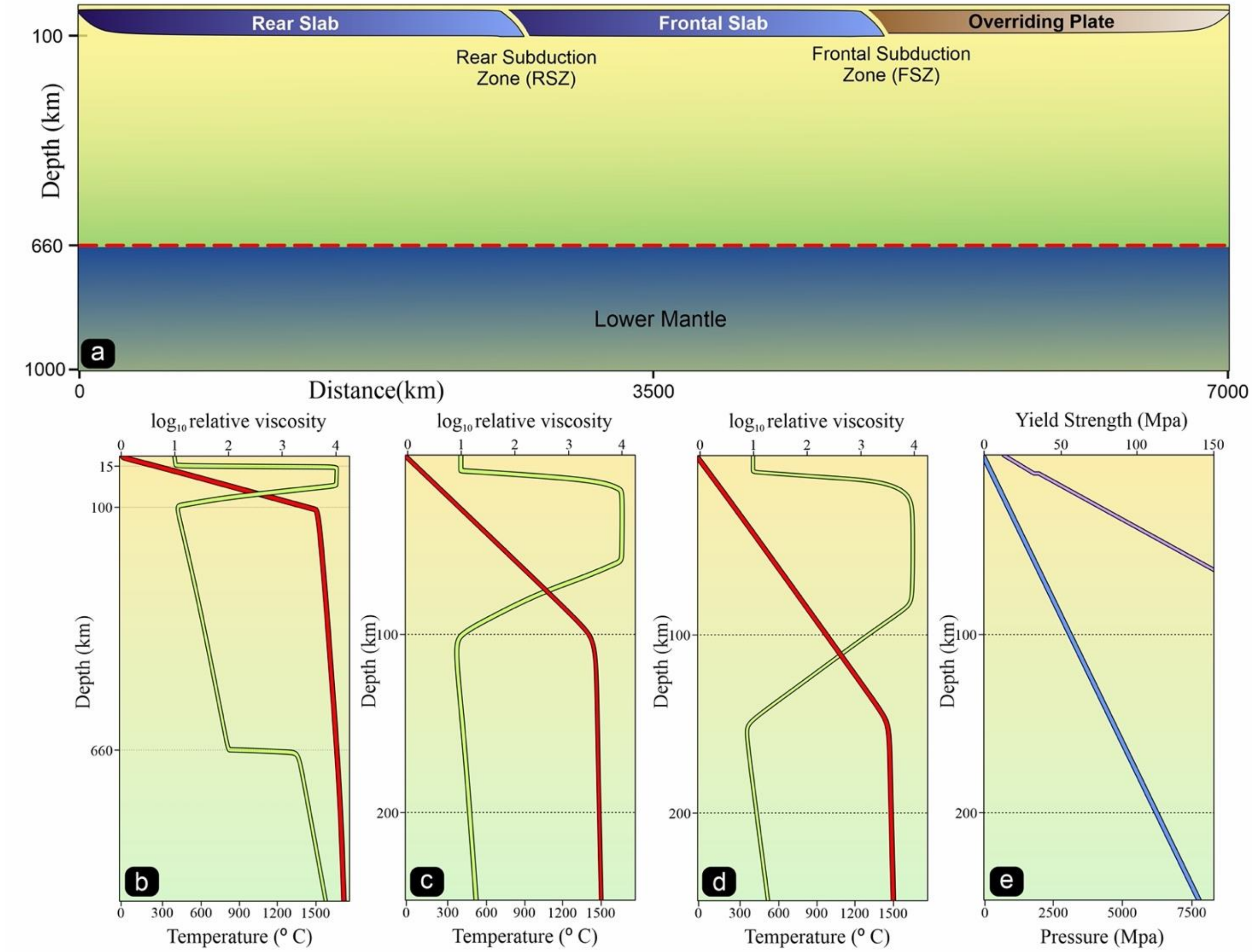

Figure 2: (a) The model setup and boundary conditions considered for CFD simulations, which shows the whole domain and initial setup of model employed for simulating same-dip double subduction in oceanic setting. Detailed illustrations representing the viscosity and temperature profiles of b) the complete model domain, c) oceanic lithosphere, and d) continental lithosphere utilized in the models. The viscosity values are relative to the asthenosphere value of 10^{20} Pa s. e) The strength plots exhibiting depth-dependent variations, showcasing increasing strength (purple) and pressure (blue).

Basin (Stevens et al., 2020). To investigate the mechanical effects of pre-existing micro-continents, the model includes a 150 km thick continental lithospheric block (containing 40 km continental crust) between two oceanic plates. The continental lithosphere is assigned a compositional density lower than that of mantle material by 600 kg/m^3. All the rheological and thermal parameters used in this study are summarized in Table 1.

2.2. Model Configurations

Natural subduction zones occur in various convergent tectonic settings, which can be broadly categorized as: 1) oceanic settings (e.g., Izu-Bonin-Mariana), where two or more oceanic plates converge to each other; 2) ocean – continent settings (e.g., the Andean subduction system), where oceanic plates converge against continents; and 3) continent-continent settings (e.g. the Indo-Eurasia collisional zone), where two or more continents converge to each other. Observations of the Earth's present-day plate structures reveal that SDDS systems can develop in any of these three tectonic settings, giving rise to a spectrum of their potential plate configurations. Based on the paleo-reconstructions of the Neo-Tethyan tectonics, we thus chose three different cases for the model settings, with an objective to investigate the mode of double-subduction evolution depending on the initial plate architecture. Each of these initial setting accounts for local lithospheric weaknesses in a specific arrangement with or without mechanically strong continental blocks.

The first case of our subduction modelling (referred to as *oceanic plate model*) replicates a simple oceanic plate tectonic setting, consisting of a 120 Ma old, flat lying oceanic lithosphere with an initial length of 5000 km (Fig. 3a). The model initially contains two similarly dipping narrow mechanically weak zones in the oceanic lithospheric plates at distances of 2500 km and 5000 km. The second case (referred to as *oceanic– continental plate model*) is designed to represent an ongoing subduction system, where an oceanic plate has already been subducted into the upper mantle, carrying a microcontinental block of 400 km long and ~150 km thick (Fig. 4a). The block is assumed to form a weak interface with the adjoining oceanic plate, possibly resulting from the inter-plate 3D differential stress localization (Auzemery et al., 2020; Heidbach et al., 2007). On the rear side, it is separated from an 80 Ma old oceanic lithosphere by a dipping (30º) weak zone. The third model, designed to reproduce a continent-continent collisional setting (referred to as *multiple continent model*), initially consists of a flat-lying, 1200 km long 80 Ma old oceanic lithosphere, and two continental blocks (thickness: 150 km and length: 1500 km), separated by an oceanic basin. This oceanic plate forms a narrow weak channel at the contact with the overriding strong continental plate (Fig. 5a). The continental blocks are compositionally buoyant relative to the underlying asthenosphere (Fig. 2d).

3. Model results

3.1. Oceanic plate settings

In this type of model architecture, plastic yielding localizes preferentially at one of the pre-existing lithospheric weaknesses (Fig.3a), resulting in an unstable mechanical state of the flat-lying oceanic plate to trigger and initiate the rear subduction zone (RSZ). The subduction initiation is coupled with formation of a spreading centre (divergent tectonics) that eventually acts as a new active site of oceanic plate generation. At ~6 Myr, the newly generated lithosphere constitutes a well-developed overriding plate (OP) structure in the subduction zone. The proto-slab subducts to a depth of ~300 km with a convergence rate (V_C) of ~ 13 cm/yr (with respect to its adjoining overriding oceanic plate) on a model run time of 8.1 Myr (Fig 3b). The RSZ oceanic plate, which is tectonically the most active unit at this stage, approaches the trench with a velocity (V_P) of ~+12 cm/year (+ sign denotes movement towards the right), while the trench itself retreats with a velocity (V_{RT}) of ~-2.5 cm/yr. The plate convergence velocity (V_C), calculated between passive marker 1 and 3 (Fig. 3a), accelerates further with increase in the total negative buoyancy to attain a maximum value of~15 cm/year at ~8 Myr (Fig. 6a), and with the RSZ slab dip (at 125 km depth) steepening to ~45°. At a model run time of 10.1 Myr, the slab encounters the lower mantle at a depth of 660 km and decelerates ($V_P \approx 7.5$ cm/yr) due to higher viscous resistance offered by the

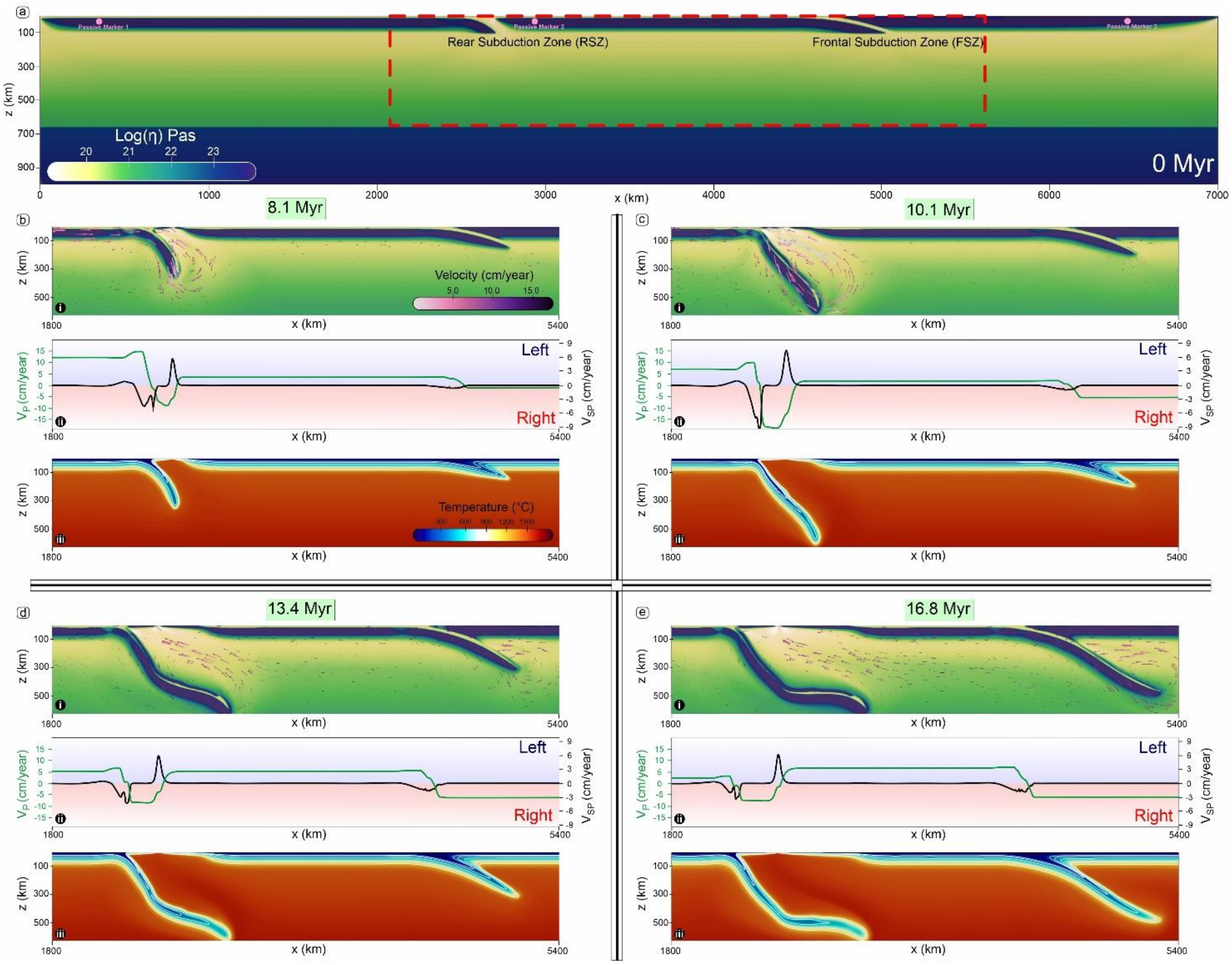

Figure 3: Evolution of the double subduction model in an oceanic setting. Panels show: (a) the initial viscosity field of the complete numerical model domain, (b)-(e) evolution of the i) viscosity and velocity fields, ii) plate velocities (green) and subduction velocity (black), and iii) temperature field, zoomed into a region around the subduction zone for four time-steps corresponding to the back subduction initiation (*t*= 8.1 Ma), frontal subduction initiation (*t*= 10.1 Ma), frontal subduction free sinking (*t*= 13.4 Ma) and mature double subduction (*t* = 16.8 Ma) phases.

strong lower mantle. This slab-lower mantle interaction also forces the oceanic plate to slow down its convergence motion (Vc ≈12 cm/year) (Fig. 6a), prompting the other proto-slab to activate its subduction motion and result in the initiation of the frontal subduction zone (FSZ) (Fig. 3c). At this stage of plate evolution the tectonic setting transforms into a typical double-subduction configuration, albeit with significant asymmetry in terms of both slab geometry and kinematics, where the FSZ slab shows much shallower dip (20° at 125 km depth) and lower convergence velocity ($V_c^{RS} \approx 7$ cm/yr) than the rear subducting slab. Additionally, the RSZ trench retreats significantly faster ($V_{RT} \approx 9$ cm/yr) than the FSZ trench ($V_{FT} \approx 2.5$ cm/yr). The cumulative effects of double-subduction motion facilitate the convergence velocity (Vc) to not only attain but also sustain extremely high values for a prolonged period of time (~6 Myr). This is in stark contrast to scenarios of single subduction, where such extreme convergence rates only can prevail over relatively short durations (< 1 Myr).

The double-subduction system always maintains an active state of the spreading centre, which in turn continues to produce new lithospheric materials. At ~13.4 Myr, the RSZ verges to a declining stage, marked by a significant drop in V_P (~5 cm/yr), although its trench continues to retreat with $V_{RT} \sim 3$ cm/yr. In contrast, the FSZ continues to remain active, where the subducting slab sinks rapidly into the upper mantle to facilitate the convergence velocity ($V_P \approx 5$ cm/year) as well as the trench retreat velocity ($V_{FT} \approx 7$ cm/year). However, the SDDS system cumulatively shows a decreasing trend of the net plate convergence velocity ($V_c \approx 11$ cm/yr). At ~16.8 Myr, the rear subducting slab moves backward as V_{RT} (~3.5 cm/year) exceeds V_P (~2.5 cm/year) and the double-subduction evolves to a steady state condition of the RSZ in terms of V_c and slab dip (~55°). On the opposite side however, the oceanic plate associated with the FSZ attains a maximum velocity $V_P \approx 6.5$ cm/year, which is significantly higher than the rear subducting plate velocity. The FSZ slab then moves through the entire upper mantle to encounter the lower mantle and eventually slows down its velocity. The corresponding trench continues to retreat with $V_{FT} \approx 6$ cm/yr, which subsequently surpasses the FSZ plate velocity in course of the subduction evolution (>20 Myr). The total convergence velocity attains a steady configuration with a constant velocity of ~8.5 cm/year which continues to the end of the model run.

The interplay of subduction-induced mantle circulation significantly governs the dynamic conditions within convergent margins. During the stage of the RSZ initiation, the flow induced by the descending slab exhibits both vertical and horizontal components, shaping a circulating flow vortex around the subducted slab. The vortex remains active till ~10Ma, gradually waning as the RSZ slab decelerates upon encountering the 660 km discontinuity. As this deceleration occurs, the vortex's focal point shifts to the FSZ slab, accompanied by an increasing intensity of flow over time. At ~13 Myr, the double-subduction configuration ushers in a potent upward flow parallel to the slabs beneath the spreading centre. This sub-lithospheric flow gains further strength by merging with the counter-flow generated by the frontal subducting slab (Fig. 3e-i). Together, these components constitute a robust mechanism for channelling mantle material towards the spreading centre. Notably distinct from typical single-subduction driven corner and wedge flows, this increased supply of mantle materials emerges as a pivotal factor in driving the accretion rates of the lithosphere. Its impact on lithospheric accretion proves to be profound, setting it apart as a distinctive and influential feature in the context of SDDS.

3.2. Microcontinent - oceanic plate setting

The micro-continent-bearing oceanic plate setting consists of an already initiated subduction in the front (FSZ: frontal subduction zone) and the lithospheric weakness between the microcontinent and the oceanic plate results in the initiation of the rear subduction zone. This results in the formation of a double-subduction system at an early stage (~ 6 Myr) of the model run (Fig.4b), as evident from a convergence velocity V_C = ~5 cm/yr (Fig. 6b). The subduction zones, however, grow at different rates, where the FSZ subduction is much more active than the RSZ. This difference in the subduction rates leads to activation of a rift between the FSZ oceanic plate and the microcontinent. The rift subsequently acts as a spreading centre, allowing upwelling

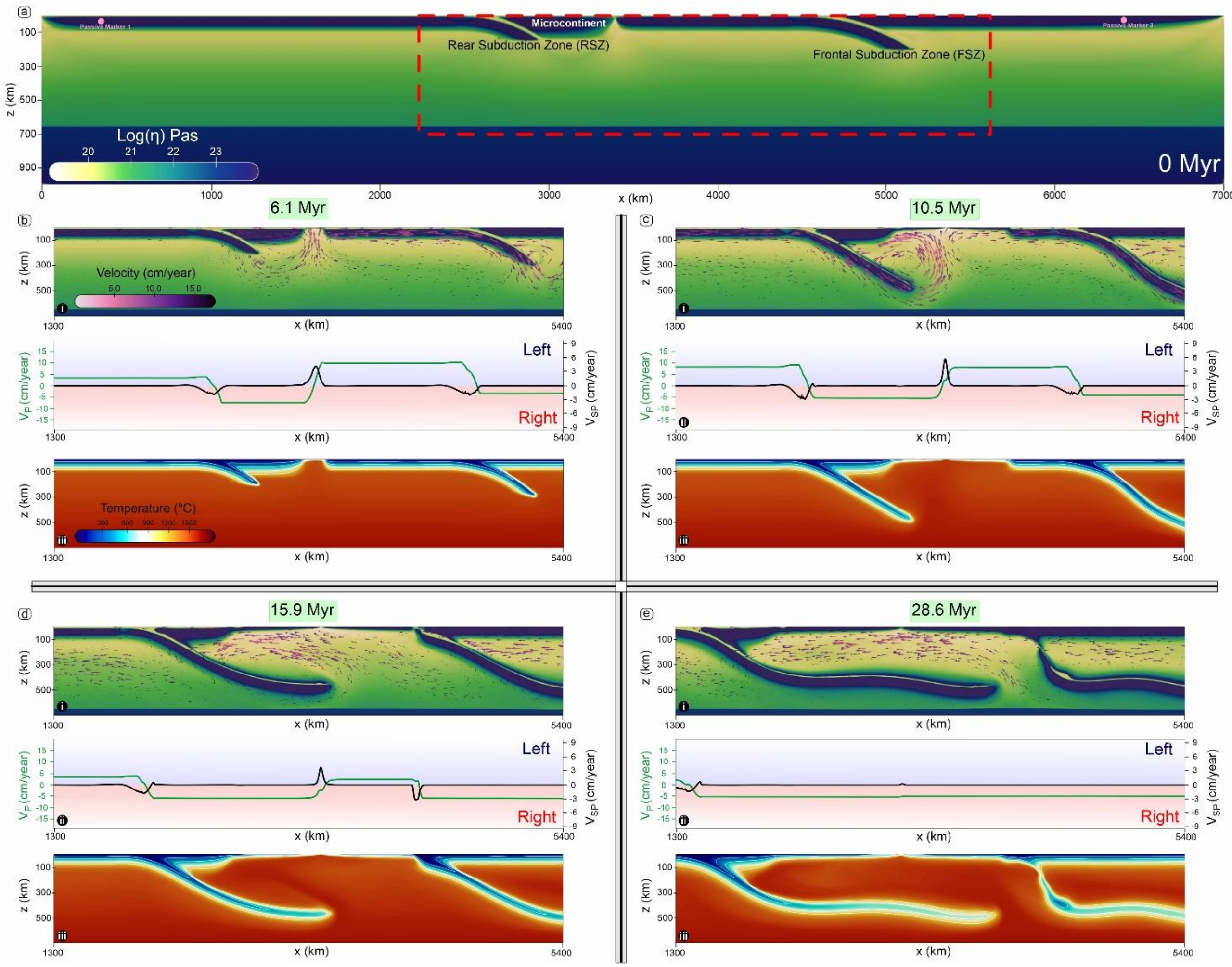

Figure 4: Evolution of the double subduction model in presence of a continental block. Panels show: (a) the initial viscosity field of the complete numerical model domain, (b)-(e) evolution of the i) viscosity and velocity fields, ii) plate velocities (green) and subduction velocity (black), and iii) temperature field, zoomed into a region around the subduction zone for four time-steps corresponding to the fore subduction free sinking (*t*= 6.1 Ma), back subduction free sinking (*t*= 10.5 Ma), mature double subduction (*t*= 15.9 Ma) and fore subducting slab detachment (*t* = 28.6 Ma) phases.

of the underlying mantle material to the surface and generate new oceanic lithosphere between the continental and the frontal oceanic plates. At ~ 6.1 Myr, the RSZ proto-slab subducts to a depth of ~200 km into the upper mantle, and this subduction motion forces the continental block to act as an OP, moving trench-ward at a velocity $V_P \approx$ -7 cm/year. The FSZ slab, on the other side, continues to subduct freely into the upper mantle, setting the entire plate to move at a high velocity ($V_P \approx$+10 cm/yr) (Fig. 4a). During this phase of tectonic evolution both the trenches retreat, but with contrasting velocities; the RSZ trench retreats at a much faster rate ($V_{RT} \approx$ -6.5 cm/yr) than the FSZ ($V_{FT} \approx$ -3.8 cm/yr). The convergence velocity (V_C) between the main OP and the RSZ slab is ≈7 cm/year, which increases to attain a high value ($V_C \approx$13 cm/yr) on a model run time of ~9 Myr (Fig. 6b). The frontal oceanic slab reaches the lower mantle at ~ 10.5 Myr, and begins to slow down its velocity ($V_P \approx$+7 cm/yr) as it encounters higher viscous forces in the 660 km transition zone. The RSZ slab, however, continues to subduct through the upper mantle and maintains the rear oceanic plate movement at a velocity of ≈ +8 cm/year. The RSZ trench at the same time retreats, but with a reduced velocity ($V_{RT} \approx$-5 cm/yr), whereas the FSZ trench continues to retreat at a steady rate ($V_{FT} \approx$ +4 cm/year). The convergence velocity is high ($V_C \approx$13 cm/year) although it begins to show a diminishing trend after this period. On a model run time of ~15.9 Myr, both the subducting oceanic slabs lower their dips to become almost flat, and significantly reduce the plate velocities ($V_P \approx$ +2.5 cm/yr and ≈ +3.5 cm/yr for FSZ and RSZ slabs, respectively). The relatively buoyant juvenile (~15 Myr) lithosphere, formed at the spreading centre, eventually reaches the FSZ trench and its subduction accelerates the retreat motion ($V_{FT} \approx$+7.5 cm/year). This motion reduces its slab dip from 30° to ~26° (Fig. 6b), which starts to increase exponentially after ~18 Myr. The RSZ trench retreat velocity (V_{RT}) increases to -5.5 cm/yr during this period. At ~25 Myr, the FSZ slab undergoes break-off at the location of maximum strain localisation developed by the negative buoyancy induced slab pull (see Supplementary S1 for detailed strain-rate plots).

In this SDDS system, the spreading centre located between the two trenches remains active, continuously adding new lithosphere to accommodate the increasing space between the continental block and the frontal oceanic plate. At ~28.6 Myr, the spreading centre, however, becomes almost inactive as the upwelling process is replaced by slab-driven horizontal flows in the mantle region between the two subducting plates. The entire newly formed lithosphere is coherently coupled with the main OP, as revealed from the plate velocity ($V_P \approx$ -5 cm/year). The double subduction system ceases to exist due to the absence of slab pull force at the FSZ trench and transforms into a single subduction system.

3.3. Multiple-continental plate setting

The modelling of a multiple-continental setting primarily aims to investigate the influence of continental plates on the process of subduction initiation and evolution, leading to the formation of a double-subduction system. The model run shows that subduction localize preferentially along the lithospheric weakness and initiates the frontal subduction zone (FSZ), leaving the trailing weak zone at the continent-oceanic plate interface almost inactive (Fig. 5b). At this stage (~ 4 Myr) the system follows mostly single-subduction dynamics, allowing the FSZ slab to penetrate into the upper mantle to a depth of ~200 km. This plate velocity (V_P) increases to ~+7.5 cm/year on a model run time of 8.5 Myr (Fig. 5b). The velocity field indicates that the lithospheric plates move coherently as a single unit to subduct beneath the FSZ trench although a lithospheric weakness is present in between them ($V_P \approx$+5 cm/year for rear oceanic plate). This implies that the FSZ entirely determines the dynamics of the system at an early stage. The frontal oceanic plate progressively accelerates its motion to attain a convergence rate ($V_c^{RS} \approx$ 8 cm/year, Fig. 6c solid blue line) with respect to the OP at ~11.5 Myr. At this stage the subduction system undergoes a remarkable kinematic transformation, leading to plate decoupling at the rear lithospheric weakness that eventually triggers mantle upwelling and accretion of new lithospheric materials to form a thin overriding plate. This decoupling decelerates the rear plate motion ($V_P \approx$+1 cm/year) and brings it almost to a halt. In contrast, the frontal slab continues to maintain a high plate velocity ($V_P \approx$ +7.5 cm/year) and a high convergence rate (V_c^{RS} = +7.5 cm/year), along with a moderate trench retreat rate ($V_{FT} \approx$-3.5 cm/yr). At ~ 12.5 Myr, the rear subducting slab gains significant a slab-pull velocity

(V_{SP} ≈ -10 cm/year), which consequently causes the rear subduction zone (RSZ) to initiate. The proto-slab continues to move through the upper mantle, setting the convergence velocity rapidly accelerate to attain a value of ~11 cm/year at 13.8 Myr. On the other side, the FSZ slab reaches the 660-km transition zone and slows down its overall sinking velocities. The continental block in this plate reaches the trench and collides with the overriding plate, switching a reversal in the trench motion to advance at a rate V_{FT} ≈+2 cm/yr. The collision event also reduces the plate velocity (V_P ≈ +5 cm/yr) as well as the convergent velocity (V_c^{RS}≈ 4.5 cm/yr) at ~15 Myr. Eventually, the RSZ

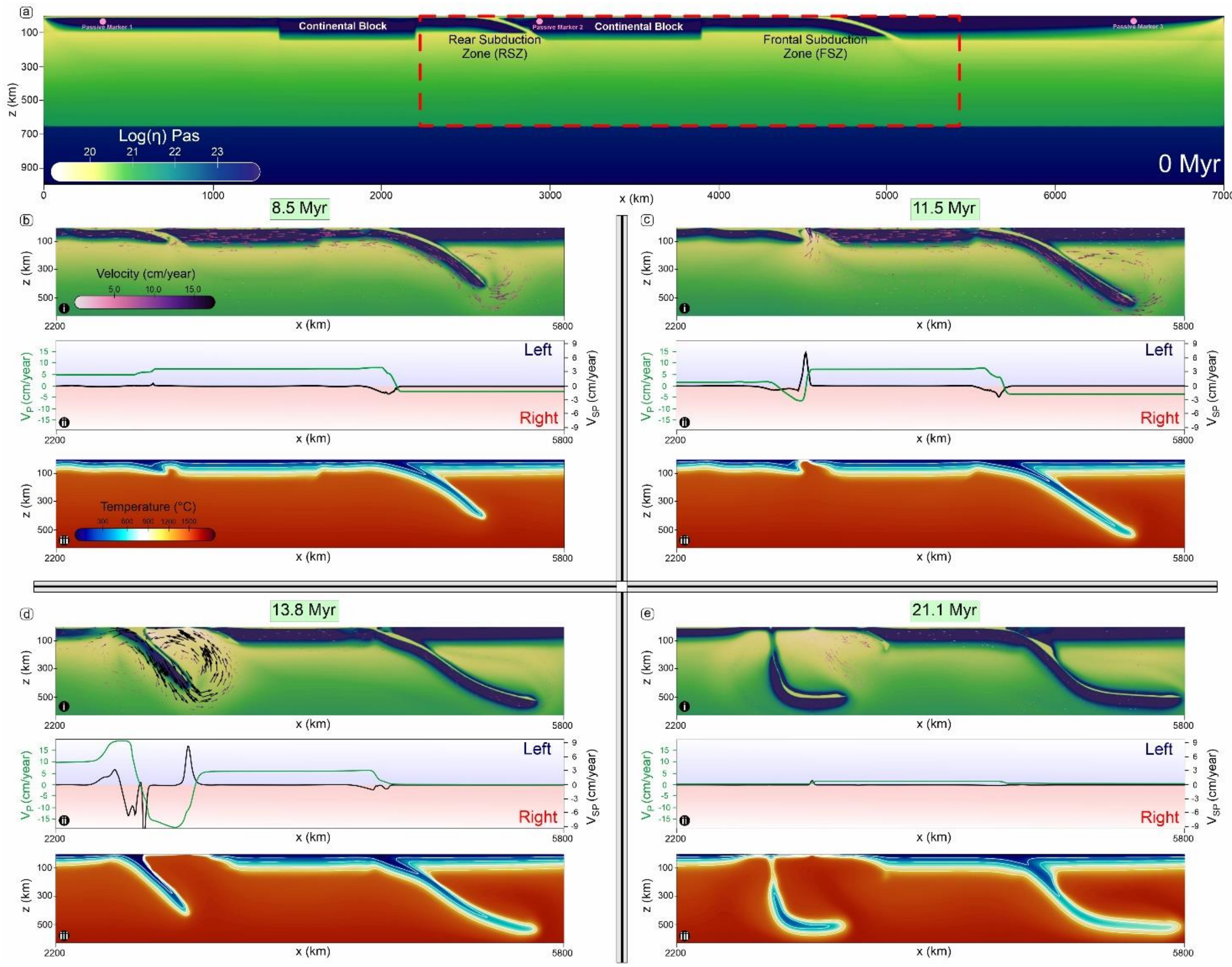

Figure 5: Evolution of the double subduction model in presence of multiple continental plates. Panels show: (a) the initial viscosity field of the complete numerical model domain, (b)-(e) evolution of the i) viscosity and velocity fields, ii) plate velocities (green) and subduction velocity (black), and iii) temperature field, zoomed into a region around the subduction zone for four time-steps corresponding to the fore subduction free sinking (t= 8.5 Ma), continental collision (t= 11.5 Ma), back subduction initiation(t= 13.8 Ma) and back subducting slab detachment (t= 21.1 Ma) phases.

experiences strong extensional forcing created by the FSZ, and its convergence reduces to extremely low rates, which impedes the trench retreat, causing the RSZ slab to steepen (> 65º at 125 km) and eventually break off. The continental block plays an instrumental role to facilitate triggering the slab detachment at ~ 16 Myr. In course of the double-subduction evolution (~21.1 Myr), the plate velocities drastically drop to ~ 2.5 cm/year and the tectonic setting transforms into a single subduction system. Thus these results show that in this SDDS system, two simultaneous subduction zones cannot be sustained and the subduction behind the collision zone ceases without

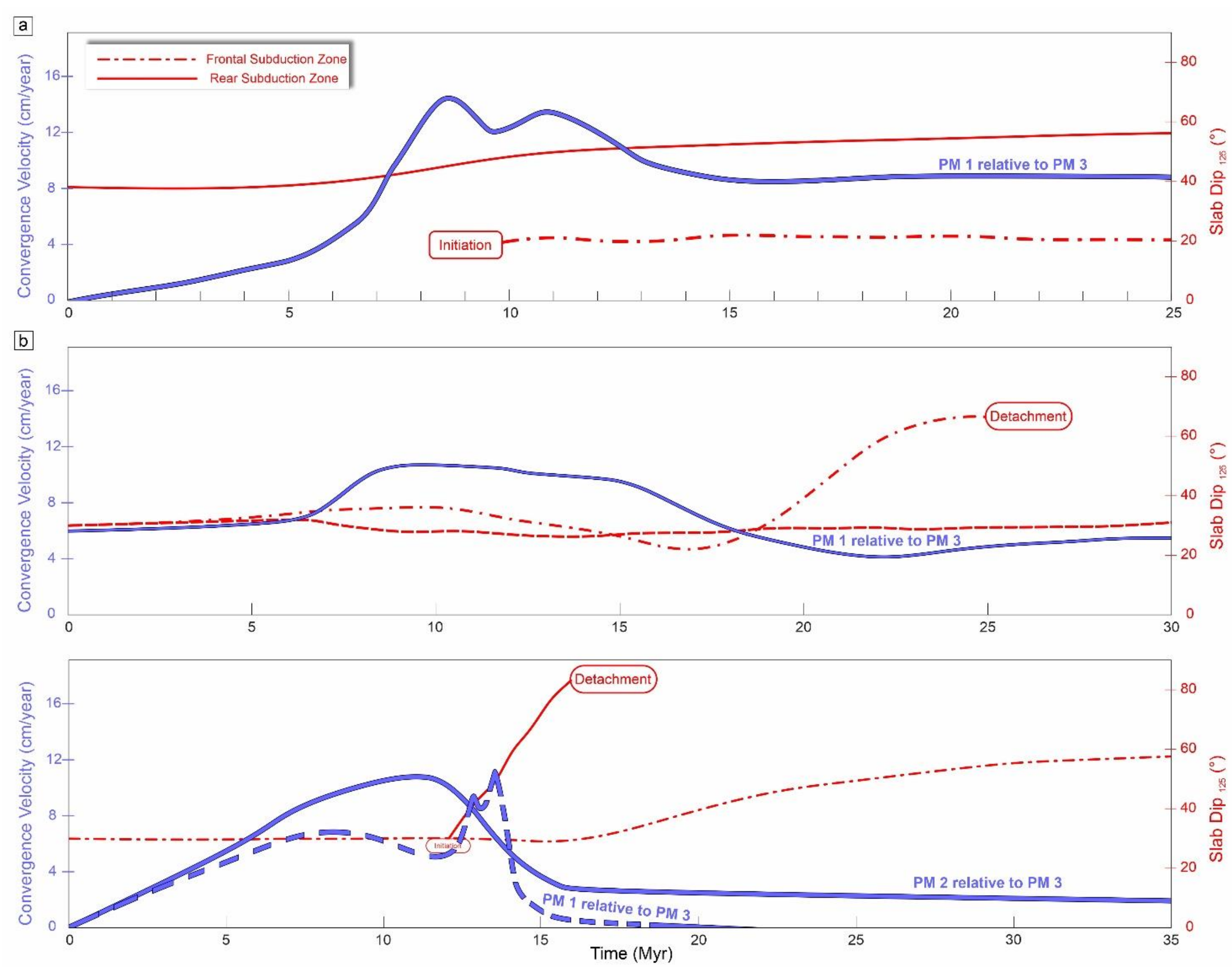

Figure 6: Temporal evolution of subduction zone convergence rates and shallow slab dips (at depth = 125 km) of fore and back subducting slabs, for double subduction in a) oceanic setting, b) microcontinent - oceanic plate setting and, c) multiple continental plate setting. PM: Passive Marker

attaining maturity.

4. Discussion

4.1. *Applicability of the double-subduction models to the Neo-Tethyan systems*

Based on the available field, petrological, paleo-magnetic and geochemical information, we consider the following Neo-Tethyan subduction systems: i) Trans-Tethyan intra-oceanic system, ii) India-Andaman-Burma subduction system, and iii) Amirante-India-Eurasia to discuss their evolution in the light of the present SDDS models. These subduction systems are chosen as their plate tectonic settings have been well-constrained by combining geological and geophysical observations in recent studies.

4.1.1. Cretaceous evolution of the Trans-Tethyan System

The Trans-Tethyan intra-oceanic system (Fig. 7a) evolved through multiple subduction episodes in the Neo-Tethys during the Cretaceous to Early Tertiary period as discussed earlier in Section 1. The convergence history, derived from the plate reconstructions and paleomagnetic

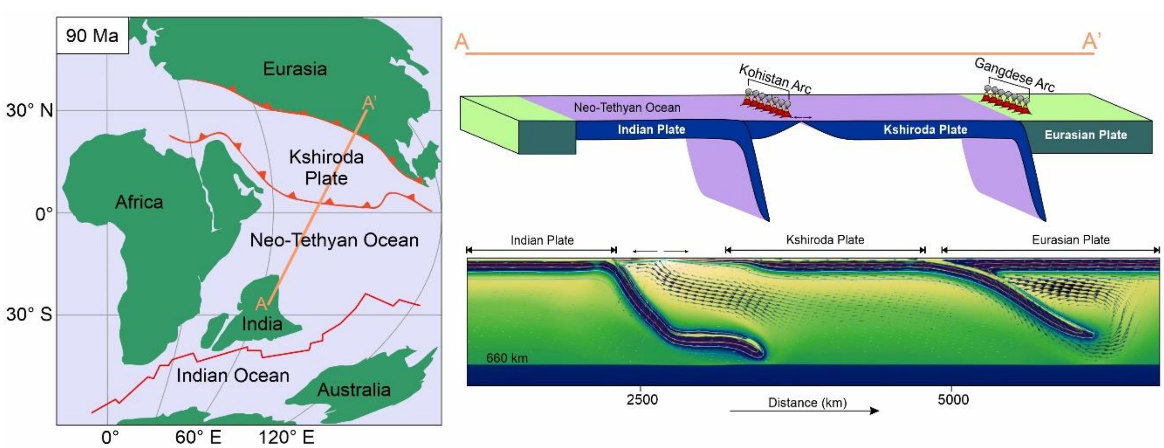

Figure 7: a) Sketch showing the reconstructions of Neo-Tethyan plate boundaries at ~90 Ma modified after Jagoutz et al., 2015 b) Cross section along AA' showing slab geometries and distances between the two prominent subduction systems giving rise to the double subduction process. c) Time snapshot (16 Myr) of the oceanic SDDS model which simulates the Cretaceous evolution of the Trans-Tethyan System.

interpretations (Cande and Stegman, 2011; Copley et al., 2010; Van Hinsbergen et al., 2011) reveal that, during the Indo-Eurasian convergence the Indian Plate had a rapid northward drift moving at extremely high rates > 12 cm/year from 60 Ma to 50 Ma (Copley et al., 2010; Molnar & Stock, 2009), which subsequently reduced to 8 cm/year at ~40 Ma that marks the timing of India-Eurasia collision (Maiti et al., 2021). Our oceanic plate model presented in Section 3.1 provides new insights into the geodynamic evolution of the Trans-Tethyan intra-oceanic system. The subducting oceanic plates in the model RSZ and FSZ represent the frontal oceanic part of the Indian Plate and the Kshiroda Plate, respectively, in association with the Eurasian overriding plate (Fig 7a,b). Pre-existing lithosphere-scale weaknesses, such as transform faults or oceanic fracture zones between the Kshiroda and the Indian Plate nucleated the subduction initiation at the leading edge of the Indian oceanic lithosphere, almost synchronously accompanied by opening of a proto back-arc extensional zone. The subduction event resulted in arc formation, preserved as the Kohistan-Ladakh Arc in the Himalaya-Tibet Mountain system (Bouilhol et al., 2013). A correlation of the arc initiation timing with the paleomagnetic data reveal that the Kohistan–Ladakh Arc rocks and ophiolites in the Tsangpo-suture zone formed nearly at the equator position (Aitchison et al., 2000). After ~4 - 5 Myr from the intra-oceanic subduction initiation, the passive margin between the Kshiroda and Eurasian Plates became active to form a second subduction (FSZ) (Fig. 7c), which gave rise to the Gangdese-Karakoram continental arc. The paleomagnetic data of magmatic rocks indicate that the arc formed at a latitudinal position ~20°–25° N, suggesting a distance of ~2500 km from the Kohistan Arc, which is consistent with the present model estimates. The model convergence history reveals a period of rapid convergence with velocities > ~15 cm/year for a period of ~8 Myr before reducing to ~9 cm/year in the later phase of the model run. This two-stage kinematic evolution is also in agreement with the Cretaceous convergence history of the Indo-Eurasian system prior to the Early Cenozoic slowdown (Molnar and Stock, 2009).

4.1.2. Cenozoic evolution of the Andaman System

In the case of the Andaman Subduction System (Fig. 8a, b), the active subduction occurs currently at the northern flank of the Java trench where the oceanic part of the Indian Plate subducts at a low angle to the arc-trend beneath a small continental block as the overriding plate (Fig. 5). This continental fragment, which is a detached part of the larger Indian Plate occurs parallel to the

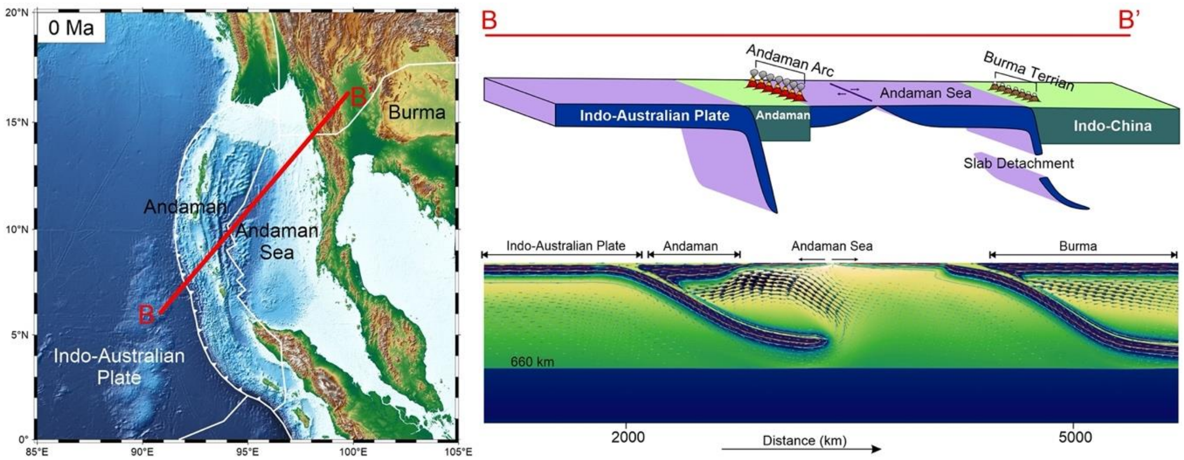

Figure 8: a) Bathymetric map of the Andaman Subduction Zone b) 3D block diagram of important components in the present-day Andaman–Nicobar subduction system along the BB' profile showing slab geometries and spatial relation between the two subduction systems and the Andaman micro-continent. c) Time snapshot (15 Myr) of the oceanic-continent double subduction model which simulates the last 30 Myr evolution of this eastern Neo-Tethyan region.

volcanic arc, forming the Andaman Island Chain. The Pliocene-Holocene volcanism in the inner arc of the Java Trench suggests that the subduction has remained active since the late Miocene (Acharyya et al., 1991; Sengupta et al., 1990). The Andaman Sea, a manifestation of extensional tectonics and other similar basins in this region also opened up in the late Miocene (Curray, 2005). The Andaman Ophiolites occur in a flat-lying arrangement, showing a close spatial association with a zone of negative gravity anomalies that suggest their occurrence as thin sub-horizontal bodies. Moreover, the ophiolite suits range in age between late Mesozoic and early Eocene, much older than the Andaman Sea crust. These observations indicate that the Andaman and other related ophiolites farther north in this convergent zone were derived from a suture to the east during late Oligocene time and emplaced as nappes during the middle Eocene. The geochronological order indicates the existence of a second subduction zone at the time of late-Miocene subduction (continuing to present day) and opening of the Andaman Sea (Khan & Chakraborty, 2005). Our micro-continent - oceanic plate model (Fig. 4) explains how the SDDS dynamics controlled such a tectonic evolution in the Andaman convergent belt. The FSZ simulates the mid-Eocene subduction event where the Indo-Australian oceanic lithosphere continued to subduct beneath the Burma Plate (equivalent to the stiffer OP in the model). The model setup produces a spreading centre (extensional zone) as a consequence of some pre-existing lithospheric flaws, switching a remarkable change in the course of the general single-subduction system. The opening of this extensional zone led to the late Miocene emergence of the Andaman Sea basin. The microcontinental fragment (Andaman continental block in nature) eventually decoupled itself from the ongoing subducting slab, and initiated a second subduction in the same region, as observed in our model run time of ~6 Myr (Fig. 8c). The newly formed subduction can be compared with the presently active Indo-Australian oceanic subduction below the Java Trench. The model suggests that both the subduction remained active for a considerable time (~24 Myr), and facilitated the Indo-Australian Plate motion relative to the Burma Plate. With time, the younger oceanic lithosphere formed at the Andaman Sea spreading centre drifted to the trench close to the Burma Plate and resulted in oceanic slab detachment as the lithosphere failed to gain density required for the mid-Eocene subduction.

4.1.3. *Post-Cretaceous Indo-Eurasian Convergence*

The India-Eurasia convergence during the Cenozoic period had a collision between continental India and the Kohistan arc (Burg, 2011) and subsequently, with the Gangdese-Karakoram continental arc, resulting in the closure of the Neo-Tethyan basin. The opening of the Carlsberg Ridge in the Indian Ocean basin characterises the region south of the Indian continent (Fig 9c).

The multiple continent – oceanic plate model reproduces the Cenozoic Indo-Eurasian collisional tectonic history very well. It is worth noting that the model aims to reproduce the collision of the Indian continental plate with the Kohistan Arc (*ca* >60 Ma) (Ding et al., 2005, 2016; Khan et al.,

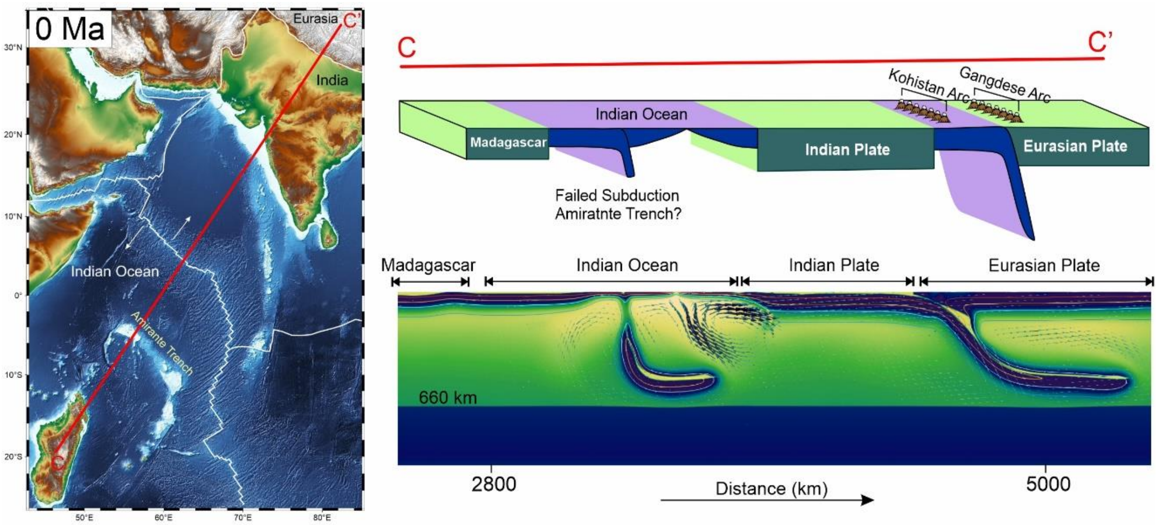

Figure 9: a) Bathymetric map of the Indo-Eurasian convergence zone and its related features b) Cross section along CC' showing slab geometries and distances between the prominent subduction features resulting in the convergence of the Indian plate with the Eurasian plate c) Time snapshot at 20 Myr of the multiple continent SDDS model which simulates the Post-Cretaceous evolution of the Indo-Eurasian collision zone.

2009) when the oceanic subduction below Eurasia was active. Interestingly, the Carlsberg ridge had a fast spreading in during late Cretaceous (Merkouriev and Sotchevanova, 2003), which is observed in our model that forms a spreading ridge and a second subduction in the ridge's vicinity. Based on our model results, we propose that the subduction occurred at the present-day position of the Amirante Trench- a trough-like feature, approximately 600 km long in the western Indian Ocean (Fig. 9a). Geological and geophysical studies show evidence of partial or limited subduction within the trench (Miles, 1982). As observed in our model, the subduction was active in this region for ~4 Myr, which ceased its activity following the slab detachment under the influence of a continental block (analogous to the Madagascar continental fragment in nature). The collision between the Indian and Eurasian continents led to a dramatic shift from retreating to advancing trench motion and a decrease in the Carlsberg ridge spreading rate, both of which are compatible with the model results.

4.2. Double-subduction evolution by feedback mechanisms

Convergent plate tectonics often evolve in a complex manner, forming multiple subduction zones that mutually interact with one another during the convergent motion (Faccenna et al., 2018; Holt et al., 2017; Mishin et al., 2008). From numerical model experiments, this study shows that a double-subduction system can grow spontaneously from pre-existing weak zones (Bercovici and Ricard, 2014; Maunder et al., 2020) under slab-pull dynamics. The two subduction zones in such systems, however, evolve in a competing mode, one suppressing the other, ultimately leading to their unequal development on a million-year timescale. To illustrate this, consider our double-subduction model for an oceanic plate setting as applicable to the Trans-Tethyan System evolution during Cretaceous. The model shows synchronous initiation of subduction at two lithospheric weak zones, but one of them preferentially becomes the most active zone (subduction velocity: ~11 cm/yr), suppressing the other slab motion to remain significantly weak (~1.5 cm/yr). This competing double-subduction dynamics causes the second subduction to become more active once the first subducting slab encounters resistance at the lower mantle at 660 km. The reduced slab motion, coupled with a trench retreat motion in one subduction has a feedback effect on the second subduction in accelerating slab motion (~1.5 cm/yr to ~6 cm/yr).

The other two model settings (Figs. 4,5) show similar feedback effects on the development of double-subduction systems. In the microcontinent-bearing oceanic plate setting, analogous to that of Andaman subduction system, the double subduction processes operate almost equally (Fig. 4), forming a spreading centre between the two subduction zones. However, the new lithosphere formed in the spreading centre causes the frontal subduction zone (FSZ) to undergo slab detachment, which in turn facilitates the slab motion in the rear subduction zone (RSZ). The multiple continental plate setting also shows a time-dependent interaction between the RSZ and FSZ during their evolution. The FSZ slab motion hardly allows the RSZ to become significantly active until the slab encounters the lower mantle to slow down its motion. The RSZ slab starts to actively sink when the RSZ almost reaches the upper-lower mantle boundary after a time of ~11 Myr. The feedback direction reverses as the RSZ experiences slab detachment due to resistance offered by the continent in the rear subducting oceanic plate. The paleo-trench at Amirante is an excellent example of subduction that failed to attain maturity due to the influence of the Madagascar continental plate. Thus, the model examples discussed here suggest that the SDDS systems generally evolve with a feedback relation between the two subduction zones that mutually interact with one another.

4.3. Influence of continental heterogeneities

Previous studies have shown that double-subduction systems introduce increased intricacies in maintaining the slab-pull and ridge-push force balance compared to single-subduction systems, and the complexity originates mainly from the effects of inter-slab interactions in plate bending, coupled with additional factors, contrasting plate ages, plate dimensions, rheology, and inter-slab distance (Mishin et al., 2008; Cížková & Bina 2015; Holt et al., 2017). This study identifies the presence of microcontinental blocks or continental plates in oceanic plate tectonic settings as an additional influential factor in the dynamics and stability of a double-subduction system. Microcontinents are mostly surrounded by oceanic crust, and they form by extension and breakup of continental masses, followed by plate boundary relocations. Jan-Mayen in the north-east Atlantic Ocean (Gaina et al., 2009; Peron-Pinvidic et al., 2012), Andaman in the Indian Ocean (Bandyopadhyay et al., 2020) and a number of small isolated islands around Australia (Gaina et al., 2003) are typical examples of microcontinents. Our microcontinent-oceanic double-subduction model suggests that such microcontinents play a vital role in localizing a spreading centre (location of new lithosphere generation) between the two subduction zones. The spreading centre, however, remains active for a specific time span, and its activity weakens following the slab detachment in the FSZ. This mechanism can be directly compared to the opening of the Andaman Sea extensional zone, synchronous to the initiation of the present-day subduction below the Andaman microcontinent.

Our model results show that an oceanic plate setting in the absence of any continental blocks can readily form a double subduction system, initiated by pre-existing lithospheric weak zones in the plate setting. However, the presence of a buoyant continental fragment selectively prevents the subduction zones in front of this plate to mature with time, and forces the system to evolve unequally at the two trenches. Similarly, a multiple-continental assemblage reduces the convergence rates due to their buoyancy and continent-arc collision effects, described as *transference* by Stern (2004) to show the accretion-assisted continental growth mechanism. The reducing convergence rates result in tensile stresses in the subducting slab, eventually leading to slab detachment (Fig. 5). The model results suggest that microcontinental blocks can greatly influence the evolution of subduction processes, as reported from several natural subduction systems, such as the northern Luzon, the Puysegur (New Zealand) and the Andaman subduction zones (Bandyopadhyay et al., 2020; Zhu et al., 2023). The microcontinents provide a potential location of passive continental margin that transforms into a tectonically active region by subduction initiation as evident in the evolution Andaman subduction system discussed above. Due to their lower mechanical strength, compared to that of large continental plates they localize subduction and facilitate the process to occur at faster rates.

4.4. Subduction-driven spreading centres: location of new plate generation

Oceanic plates subduct beneath overriding plates of different mechanical characteristics, ranging from neutrally or positively buoyant thick continental plate to negatively buoyant thin oceanic plates. Single-subduction systems generally involve slab rollback, which is often accommodated by horizontal extension and formation of a spreading center (back-arc basin) in the overriding plate. Double-subduction systems in an oceanic plate setting, on the other hand, forces the rear trench to retreat at fast rates as the frontal plate moves in the opposite direction, offering less resistance to the rear slab. This kinematic state results in formation of a spreading centre at the rear trench, which eventually acts as a site for new lithosphere generation. This mechanism allows the RSZ to accommodate slab roll back without involving overriding plate kinematics, as in a single-subduction setting. This model study thus brings out the importance of such spontaneous spreading centre formation in the SDDS evolution within large oceanic plates.

Our models demonstrate that spreading centres crucially control the subduction dynamics in transforming a double- to a single-subduction system. The microcontinent-oceanic plate model shows the development of large tensile stresses in the region between the older subducting plate and the newly formed lithosphere at the trench, which causes the older slab to experience detachment. The slab break-off eventually stops the subduction activity, leaving the other subduction active. Spreading centres also play an important role in the onset of convergent setting and promotes decoupling in a large oceanic plate (e.g., *oceanic plate model,* Fig. 3). Such tectonic processes are observed in other natural systems, for example, the Cocos-Nazca spreading centre where the spreading centre formed by splitting of the oceanic lithosphere, giving rise to the Farallon plate break up in the early Miocene.

5. Conclusions

The key results of this research are two-fold: firstly, it unveils the intricate mechanisms governing the development of same-dip double subduction (SDDS) systems. Secondly, it provides new insights into the role of SDDS dynamics in the Neo-Tethyan tectonic evolution. The principal findings of this study are summarized as follows: 1) SDDS are initiated spontaneously in presence of lithospheric-scale mechanical weaknesses, e.g., faults, without any aid of kinematic perturbations, in contrary to that suggested in earlier studies. Throughout the temporal progression of a SDDS system, the two subducting slabs mutually affect their kinematics and subduction-driven flow patterns in the mantle wedges as well as asthenosphere. 2) SDDS systems can remain active for a long period of time (>25 Myr) in an oceanic setting, and eventually attain exceptionally high convergence velocities, 16-17 cm/year during its extended period (~5 Myr) of activity, depending on the slab ages at the trenches. These model findings explain the development of a self-sustaining SDDS responsible for the anomalously Indo-Eurasian high-convergence velocity condition in the Cretaceous Neo-Tethyan evolution. 3) The presence of continental blocks in the initial plate setting greatly influences the SDDS dynamics, forcing the double subduction zones to localize preferentially at their passive margins with the oceanic plates. They grow almost equally, forming a spreading centre between the two trenches on a time scale of 25 Myr. This SDDS model accounts for the Cenozoic tectonic evolution in the eastern Neo-Tethyan region, which ultimately formed the Andaman subduction system. 4) In an initial plate configuration with multiple continental fragments or plates, the latter can cause one of the SDDS slabs to halt its motion, resulting in a double to single-subduction transformation, which occurred in the Amirante-India-Eurasia subduction system during the Cenozoic evolution of Neo-Tethys.

Declaration of Competing Interest

The authors declare that they have no known competing financial interests or personal relationships that could have appeared to influence the work reported in this article.

Acknowledgments

The work has been performed under the Project HPC-EUROPA3 (INFRAIA-2016-1-730897), with the support of the EC Research Innovation Action under the H2020 Programme; in particular, A.R. gratefully acknowledges the support of Durham University and the computer resources and technical support provided by EPCC, University of Edinburgh. A.R. gratefully acknowledges CSIR, India for awarding research fellowship grants (09/096(0940)/2018- EMR-I). This work used the ARCHER2 UK National Supercomputing Service (https://www.archer2.ac.uk). The DST-SERB is acknowledged for supporting this work through the J.C. Bose fellowship (JBR/2022/000003) to N.M.

Data Availability Statement

The authors confirm that all the data used to support the findings of this study are available within the article and as supplementary materials. All aspects of UNDERWORLD 2 (Mansour, J., et al., 2020) can be checked here (https://doi.org/10.5281/zenodo.6820562).

Description	Symbol	Unit	Default Values
Thermal expansion coefficient	α	K^{-1}	3×10^5
Thermal diffusivity	κ	m^2 s^{-1}	10^{-6}

Reference density	ρ_0	kg m^{-3}	3300
Surface temperature	T_s	K	273
Potential temperature	T_m	K	1673
Adiabatic temperature gradient	dT/dz	K km^{-1}	0.37
Gravitational acceleration	g	m s^{-2}	9.81
Maximum viscosity	η_{max}	Pa s	1.0×10^{24}
Minimum viscosity	η_{min}	Pa s	1.0×10^{19}
Crust viscosity	η_C	Pa s	1.0×10^{20}
Dislocation creep (Upper Mantle)			
Activation energy	E	kJ mol^{-1}	540
Activation volume	V	cm^3 mol^{-1}	10
Pre-factor	A	Pa^n s^1	4.1×10^{15}
Exponent	n	-	3.5
Diffusion creep (Upper and Lower mantle)			
Activation energy	E	kJ mol^{-1}	300 (UM & LM)
Activation volume	V	cm^3 mol^{-1}	4.5 (UM), 1.58 (LM)
Pre-factor	A	Pa^1 s^1	1.87×10^9 (UM)
			1.77×10^{14} (LM)
Exponent	n	-	1
Plastic yielding			

Cohesion	C_0	MPa	20
Friction coefficient	μ	-	0.1
Maximum yield stress	τ_{max}	MPa	500

Table 1: List of model parameters and their corresponding values chosen for the numerical simulations.

6. Appendix A

6.1 Governing equations

We build numerical, time-evolving, dynamically consistent thermomechanical subduction models in 2-D Cartesian domains within a theoretical framework of computational fluid dynamics (CFD), implemented by using the UNDERWORLD2 code (Mansour et al., 2020). This CFD simulation study assumes an incompressible Boussinesq fluid flow, approximated to the long-time (multi-million year) scale kinematic state of Earth's mantle. This approximation accounts for only buoyancy (body force term), treating all other effects of density fluctuations negligibly small in the momentum equation. We use the continuity and momentum conservation equations in our modelling to describe spontaneous flows in our model driven by density anomalies. The expressions of these equations are, respectively,

$$\nabla . v_i = 0 \tag{1}$$

$$\nabla . \sigma_{ij} + \rho g = 0 \tag{2}$$

where v_i is the velocity vector. In equation (2) the inertial forces are neglected, as applicable to long term flows in the mantle. σ_{ij} can be decomposed into the isotropic (${\sigma^o}_{ij}$) and the deviatoric stress (τ_{ij}) tensors as,

$$\sigma_{ij} = \sigma^{o}{}_{ij} + \tau_{ij} \tag{3}$$

such that

$$\sigma^{o}{}_{ij} = -P\delta_{ij} \tag{4}$$

$$\tau_{ij} = 2\eta\dot{\varepsilon}_{ij} = \eta\left(\frac{\partial u_i}{\partial x_j} + \frac{\partial u_j}{\partial x_i}\right) \tag{5}$$

where $\dot{\varepsilon}_{ij}$ is the strain rate tensor. Substituting Eq. (4) & (5) into Eq. (2) gives rise to the Stokes equation with pressure and velocity as two unknown variable parameters. Applying the model boundary conditions, we numerically solve the continuity and Stokes equations in a pre-defined 2D Cartesian domain to derive the velocity and pressure in the model domain.

The thermal evolution of a subduction system is dictated by combined effects of advective heat transfer, thermal diffusion, and heat sources/sinks within the system, which we tackle with the following heat equation.

$$\rho C_p \frac{DT}{Dt} = \nabla . q + \rho Q, \tag{6}$$

where Q is the rate of internal heat production per unit volume, T is the temperature, ρ is the material density and C_p is the specific heat. q represents the rate of diffusional heat transfer, described by Fourier's law as,

$$q = -k\nabla T', \tag{7}$$

where k is the thermal conductivity and T' is the nonadiabatic temperature. Substituting Eq. (7) into (6) and expanding considering the definition of material derivative, gives

$$\frac{\partial T}{\partial t} + u.\nabla T' = \kappa\nabla^2 T' + \frac{Q}{C_p} \tag{8}$$

where $\kappa = \frac{k}{\rho C_p}$, which represents the thermal diffusivity. T' is replaced by the adiabatic temperature (T_a) of the system as a function of depth (z) obtained from the relation:

$$T_a = T' + z\left(\frac{\partial T}{\partial z}\right) = T' + z\left(\frac{\alpha g T_p}{C_p}\right), \tag{9}$$

where T_p is the mantle potential temperature and α is the coefficient of thermal expansion, which was set at a value of 3×10^{-5} K^{-1}. Considering C_p = 1260 J/kg/K for Earth's mantle, a resultant adiabatic temperature gradient of 0.4 K/km is added to the nonadiabatic temperature of the mantle. The energy conservation equation (8) is solved using the Semi-Lagrangian Crank-Nicholson (SLCN) method (Spiegelman and Katz, 2006), built upon the potencies of the Crank-Nicolson scheme for diffusion and the semi-Lagrangian scheme for advection. The SLCN method has been found to be unconditionally stable, allowing large time-step sizes. We impose constant (Dirichlet) and zero-flux (Neumann) on the top and bottom boundaries, respectively to solve the energy equation. The model surface temperature is set initially at 0°C, whereas the initial model basal temperature at 1800°C.

We use half-space cooling profiles to constrain the thermal structures of model lithospheric plates corresponding to their assigned ages, considering a thermal diffusivity value of 10^{-6} m^2/s (van Hunen and Allen, 2011), and a mantle potential temperature of 1400° C (Holt and Condit, 2021). The model density parameters are chosen as a function of the assigned temperatures, taking into account the thermal properties and their evolution following the momentum equation. For temperature dependent density variations, we adopt the equation of state,

$$\rho = \rho_r\left(1 - \alpha(T - T_p)\right) \tag{10}$$

where ρ_r denotes the reference mantle density at the mantle potential temperature, which is set at 3300 kg/m^3.

6.2. Rheological considerations

We model the mantle rheology in the framework of a composite creep law that combines diffusion creep (η_{diff}), dislocation creep (η_{disl}), and plastic yielding (η_{yield}). An Arrhenius temperature and pressure dependence of the activation volume (*V*) and the activation energy (*E*) (Hirth and Kohlstedt, 2004) is chosen to describe the creep laws for mantle silicates, which leads to the diffusion/dislocation-controlled viscosity,

$$\eta_{diff/disl} = A^{\frac{-1}{n}} \dot{\varepsilon}^{\frac{1-n}{n}} exp\left(\frac{E + PV}{nRT_a}\right) \tag{11}$$

where A is a pre-factor, *n* is the stress exponent (n = 1 and 3.5 for diffusional and dislocation creep, respectively), R is the gas constant and P is the lithostatic pressure. It is usually observed that lithostatic pressure enhances the yield strength of mantle material by different stress-limiting mechanisms. In contrast, material strength can be reduced as a consequence of brittle yielding (Kohlstedt et al., 1995) near the surface. These two yield mechanisms are combined into a simplified plastic rheology (van Hunen and Allen, 2011), and the viscosity is described as,

$$\eta_{yield} = \frac{\tau_{yield}}{2\dot{\varepsilon}} \tag{12}$$

and τ_{yield} denotes the yield strength, expressed by the following relation.

$$\tau_{yield} = min\ (C + \mu P, \quad \tau_{max}) \tag{13}$$

where C (= 20 MPa) is the initial cohesion, μ (= 0.1) is the friction coefficient, and τ_{max} is the cut-off yield stress value. The harmonic mean of the three types of viscosity is considered to determine an effective model viscosity (η_{eff}),

$$\frac{1}{\eta_{eff}} = \frac{1}{\eta_{diff}} + \frac{1}{\eta_{disl}} + \frac{1}{\eta_{yield}} \tag{14}$$

The activation volumes (V) and energies (E) values (Table 1) chosen in our modelling are consistent with the experimental estimates for dry olivine (Karato and Wu, 1993). We have considered the value of pre- factor A for the upper mantle based on the following findings, 1) an effective viscosity in the order of 10^{20} Pa in the shallow part of upper mantle (Hager, 1990), and 2) seismic anisotropy implying dominantly dislocation creep in the majority part of mantle (Becker, 2006). Diffusional creep is recognized as the principal mechanism to determine the lower-mantle rheology (Karato & Wu, 1993). A range of estimates suggest its viscosity significantly higher than the upper-mantle viscosity. The calculated creep pre-factor yields a value of 3×10^{22} at the 660 km transition (Čížková et al., 2012), which increases continuously with depth (Fig. 2).

The top crustal layer in our model is assigned a constant viscosity of 1×10^{20} Pa s. We use Eq. (12) to simulate brittle failure in this layer, assuming a low value (10 MPa) of its cohesion. This rheological consideration aims to reproduce the mode crust with yield strength lower than that of the lithosphere. This modelling manipulation allows us to introduce decoupling of the subducting slab from the overriding plate and facilitate the plate convergence process. The mantle lithosphere strength is determined from the upper viscosity cut-off values (1×10^{24} Pa s), except for regions where we preferentially activate plastic yielding. For the overriding plate (OP), the upper limit of viscosity is increased to 2.5×10^{24} Pa s to obtain a slightly higher stiffness. We model the crust and the lithosphere individually single layers without any internal rheological stratification. Considering the long-term process of our present concern, the effects of elastic deformation are completely excluded. We add passive tracers in the compositional field within the regions of interest to track the plate motion and deformation during the model run.

6.3. Model Setup

We meshed the 2D domain by smaller quadrilateral elements with a mesh resolution of 512 elements in the vertical direction, which provides an element width of ~2 km, and a particle density of 50 tracers per element. These Lagrangian tracer particles used to track advecting materials and their corresponding physical properties are mapped to quadrature points with nearest-neighbour interpolation (Sandiford and Moresi, 2019). All models were subjected to g = 9.8 m/s^2, where g is the acceleration due to gravity. The model has free-slip $(v_y = 0)$ conditions assigned to the bottom boundaries, whereas periodic boundary condition is imposed on the sidewalls.

The model surface temperature is set initially at 0°C, whereas the initial model basal temperature at 1800°C. For the temperature boundary condition, we impose constant (Dirichlet) and zero-flux (Neumann) on the top and bottom boundaries, respectively to solve the energy equation. We use half-space cooling profiles to constrain the thermal structures of model lithospheric plates corresponding to their assigned ages, considering a thermal diffusivity value of 10^{-6} m^2/s (van Hunen & Allen, 2011), and a mantle potential temperature of 1400° C (Holt & Condit, 2021). The model density parameters are chosen as a function of the assigned temperatures, taking into account the thermal properties and their evolution following the momentum equation.

6.4. Numerical Scaling, Mesh Refinement Tests and Model validation

The governing equations (Section 7.1) and physical parameters are non-dimensionalized to implement them for the model simulations utilizing the UNDERWORLD2 scaling module. The model results, corresponding to the reference values of model parameters, are then scaled to their equivalent real physical units. The scaling coefficients derived from the base units of length (Kl), mass (Km), time (Kt) and temperature (KT) are set as, $Kl = 1$, $Km = \rho_{ref} \times Kl^3$, $Kt = 1 / (\frac{\eta_{ref} \times Kl}{Km})$ and $KT = T_p$, where ρ_{ref} and η_{ref} are the reference density and viscosity, respectively. The scaling strategy has been implemented to keep buoyancy force as the sole driving factor in subduction of an oceanic lithosphere, assigned a non-dimensional value of 1 to aid the solver efficiency.

We kept a mesh resolution of 1150 × 512 elements in our modelling. A set of resolution tests was performed for low (576 × 256, 288 × 128 elements) as well as for a much higher resolution (2300 × 1024 elements), with an objective to optimize the refined resolution appropriate for subduction initiation modelling and tracking the evolutionary stages of a double subduction system with thin, weak viscoplastic subduction interfaces, and a composite rheology of the upper mantle. The mesh resolutions and their effects on the trench and subducting plate (SP) velocities are detailed in the Supporting Information (S2).

References:

Acharyya, S.K., Ray, K.K., Sengupta, S., 1991. The Naga Hills and Andaman ophiolite belt, their setting, nature and collisional emplacement history. Physics and Chemistry of the Earth 18, 293–315. https://doi.org/10.1016/0079-1946(91)90006-2

Advokaat, E.L., Bongers, M.L.M., Rudyawan, A., BouDagher-Fadel, M.K., Langereis, C.G., van Hinsbergen, D.J.J., 2018. Early Cretaceous origin of the Woyla Arc (Sumatra, Indonesia) on the Australian plate. Earth Planet Sci Lett 498, 348–361. https://doi.org/10.1016/J.EPSL.2018.07.001

Aitchison, J.C., Badengzhu, Davis, A.M., Liu, J., Luo, H., Malpas, J.G., McDermid, I.R.C., Wu, H., Ziabrev, S. V., Zhou, M. fu, 2000. Remnants of a Cretaceous intra-oceanic subduction system within the Yarlung–Zangbo suture (southern Tibet). Earth Planet Sci Lett 183, 231–244. https://doi.org/10.1016/S0012-821X(00)00287-9

Arcay, D., Lallemand, S., Abecassis, S., Garel, F., 2020. Can subduction initiation at a transform fault be spontaneous? Solid Earth 11, 37–62. https://doi.org/10.5194/SE-11-37-2020

Auzemery, A., Willingshofer, E., Yamato, P., Duretz, T., Sokoutis, D., 2020. Strain localization mechanisms for subduction initiation at passive margins. Glob Planet Change 195, 103323. https://doi.org/10.1016/J.GLOPLACHA.2020.103323

Bandyopadhyay, D., van Hinsbergen, D.J.J., Plunder, A., Bandopadhyay, P.C., Advokaat, E., Chattopadhaya, S., Morishita, T., Ghosh, B., 2020. Andaman Ophiolite: An Overview 1–17. https://doi.org/10.1007/978-3-030-39843-9_1

Becker, T.W., 2006. On the effect of temperature and strain-rate dependent viscosity on global mantle flow, net rotation, and plate-driving forces. Geophys J Int 167, 943–957. https://doi.org/10.1111/J.1365-246X.2006.03172.X/2/M_167-2-943-EQ018.JPEG

Bercovici, D., Ricard, Y., 2014. Plate tectonics, damage and inheritance. Nature 2014 508:7497 508, 513–516. https://doi.org/10.1038/nature13072

Bouilhol, P., Jagoutz, O., Hanchar, J.M., Dudas, F.O., 2013. Dating the India–Eurasia collision through arc magmatic records. Earth Planet Sci Lett 366, 163–175. https://doi.org/10.1016/J.EPSL.2013.01.023

Burg, J.P., 2011. The asia-kohistan-india collision: Review and discussion. Frontiers in Earth Sciences 4, 279–309. https://doi.org/10.1007/978-3-540-88558-0_10/COVER

Cande, S.C., Stegman, D.R., 2011. Indian and African plate motions driven by the push force of the Réunion plume head. Nature 2011 475:7354 475, 47–52. https://doi.org/10.1038/nature10174

Čížková, H., Bina, C.R., 2015. Geodynamics of trench advance: Insights from a Philippine-Sea-style geometry. Earth Planet Sci Lett 430, 408–415. https://doi.org/10.1016/J.EPSL.2015.07.004

Čížková, H., van den Berg, A.P., Spakman, W., Matyska, C., 2012. The viscosity of Earth's lower mantle inferred from sinking speed of subducted lithosphere. Physics of the Earth and Planetary Interiors 200–201, 56–62. https://doi.org/10.1016/J.PEPI.2012.02.010

Copley, A., Avouac, J.P., Royer, J.Y., 2010. India-Asia collision and the Cenozoic slowdown of the Indian plate: Implications for the forces driving plate motions. J Geophys Res Solid Earth 115, 3410. https://doi.org/10.1029/2009JB006634

Corbi, F., Herrendörfer, R., Funiciello, F., van Dinther, Y., 2017. Controls of seismogenic zone width and subduction velocity on interplate seismicity: Insights from analog and numerical models. Geophys Res Lett 44, 6082–6091. https://doi.org/10.1002/2016GL072415

Curray, J.R., 2005. Tectonics and history of the Andaman Sea region. J Asian Earth Sci 25, 187–232. https://doi.org/10.1016/J.JSEAES.2004.09.001

Dasgupta, R., Mandal, N., 2018. Surface topography of the overriding plates in bi-vergent subduction systems: A mechanical model. Tectonophysics 746, 280–295. https://doi.org/10.1016/J.TECTO.2017.08.008

Ding, L., Kapp, P., Wan, X., 2005. Paleocene–Eocene record of ophiolite obduction and initial India-Asia collision, south central Tibet. Tectonics 24, 1–18. https://doi.org/10.1029/2004TC001729

Ding, L., Qasim, M., Jadoon, I.A.K., Khan, M.A., Xu, Q., Cai, F., Wang, H., Baral, U., Yue, Y., 2016. The India–Asia collision in north Pakistan: Insight from the U–Pb detrital zircon provenance of Cenozoic foreland basin. Earth Planet Sci Lett 455, 49–61. https://doi.org/10.1016/J.EPSL.2016.09.003

Eyuboglu, Y., Dudas, F.O., Zhu, D.C., Liu, Z., Chatterjee, N., 2019. Late Cretaceous I- and A-type magmas in eastern Turkey: Magmatic response to double-sided subduction of Paleo- and Neo-Tethyan lithospheres. Lithos 326–327, 39–70. https://doi.org/10.1016/J.LITHOS.2018.12.017

Faccenna, C., Holt, A.F., Becker, T.W., Lallemand, S., Royden, L.H., 2018. Dynamics of the Ryukyu/Izu-Bonin-Marianas double subduction system. Tectonophysics 746, 229–238. https://doi.org/10.1016/J.TECTO.2017.08.011

Gaina, C., Gernigon, L., Ball, P., 2009. Palaeocene-Recent plate boundaries in the NE Atlantic and the formation of the Jan Mayen microcontinent. J Geol Soc London 166, 601–616. https://doi.org/10.1144/0016-76492008-112/ASSET/666CE50E-4E50-4EA4-825A-5FD0D19C5F10/ASSETS/GRAPHIC/601FIG10.JPEG

Gaina, C., Müller, R.D., Brown, B., Ishihara, T., 2003. Microcontinent formation around Australia. Special Paper of the Geological Society of America 372, 405–416. https://doi.org/10.1130/0-8137-2372-8.405

Ghosh, B., Bandyopadhyay, D., Morishita, T., 2017. Andaman-Nicobar Ophiolites, India: Origin, evolution and emplacement. Geological Society Memoir 47, 95–110. https://doi.org/10.1144/M47.7/ASSET/B51D4277-1DC1-4B58-A0F0-AA65A51742BC/ASSETS/IMAGES/LARGE/M47-1018F08.JPG

Gürer, D., van Hinsbergen, D.J.J., Matenco, L., Corfu, F., Cascella, A., 2016. Kinematics of a former oceanic plate of the Neotethys revealed by deformation in the Ulukışla basin (Turkey). Tectonics 35, 2385–2416. https://doi.org/10.1002/2016TC004206

Hager, B.H., 1990. Mantle viscosity: a comparison of models from postglacial rebound and from the geoid, plate driving forces, and advected heat flux. Glacial isostasy, sea-level and mantle rheology 493–513. https://doi.org/10.1007/978-94-011-3374-6_23/COVER

Hall, R., 2012. Late Jurassic–Cenozoic reconstructions of the Indonesian region and the Indian Ocean. Tectonophysics 570–571, 1–41. https://doi.org/10.1016/J.TECTO.2012.04.021

Hall, R., Spakman, W., 2002. Subducted slabs beneath the eastern Indonesia–Tonga region: insights from tomography. Earth Planet Sci Lett 201, 321–336. https://doi.org/10.1016/S0012-821X(02)00705-7

Heidbach, O., Reinecker, J., Tingay, M., Müller, B., Sperner, B., Fuchs, K., Wenzel, F., 2007. Plate boundary forces are not enough: Second- and third-order stress patterns highlighted in the World Stress Map database. Tectonics 26. https://doi.org/10.1029/2007TC002133

Hirth, G., Kohlstedt, D., 2004. Rheology of the Upper Mantle and the Mantle Wedge: A View from the Experimentalists. Geophysical Monograph Series 138, 83–105. https://doi.org/10.1029/138GM06

Holt, A.F., Condit, C.B., 2021. Slab Temperature Evolution Over the Lifetime of a Subduction Zone. Geochemistry, Geophysics, Geosystems 22, e2020GC009476. https://doi.org/10.1029/2020GC009476

Holt, A.F., Royden, L.H., Becker, T.W., 2017. The dynamics of double slab subduction. Geophys J Int 209, 250–265. https://doi.org/10.1093/GJI/GGW496

Jagoutz, O., Royden, L., Holt, A.F., Becker, T.W., 2015. Anomalously fast convergence of India and Eurasia caused by double subduction. Nature Geoscience 2014 8:6 8, 475–478. https://doi.org/10.1038/ngeo2418

Jolivet, L., Faccenna, C., Becker, T., Tesauro, M., Sternai, P., Bouilhol, P., 2018. Mantle Flow and Deforming Continents: From India-Asia Convergence to Pacific Subduction. Tectonics 37, 2887–2914. https://doi.org/10.1029/2018TC005036

Karato, S.I., Wu, P., 1993. Rheology of the Upper Mantle: A Synthesis. Science (1979) 260, 771–778. https://doi.org/10.1126/SCIENCE.260.5109.771

Khan, P.K., Chakraborty, P.P., 2005. Two-phase opening of Andaman Sea: a new seismotectonic insight. Earth Planet Sci Lett 229, 259–271. https://doi.org/10.1016/J.EPSL.2004.11.010

Király, Á., Funiciello, F., Capitanio, F.A., Faccenna, C., 2021. Dynamic interactions between subduction zones. Glob Planet Change 202, 103501. https://doi.org/10.1016/J.GLOPLACHA.2021.103501

Király, Á., Holt, A.F., Funiciello, F., Faccenna, C., Capitanio, F.A., 2018. Modeling Slab-Slab Interactions: Dynamics of Outward Dipping Double-Sided Subduction Systems. Geochemistry, Geophysics, Geosystems 19, 693–714. https://doi.org/10.1002/2017GC007199

Kohlstedt, D.L., Evans, B., Mackwell, S.J., 1995. Strength of the lithosphere: Constraints imposed by laboratory experiments. J Geophys Res Solid Earth 100, 17587–17602. https://doi.org/10.1029/95JB01460

Kufner, S.K., Schurr, B., Sippl, C., Yuan, X., Ratschbacher, L., Akbar, A. s/of M., Ischuk, A., Murodkulov, S., Schneider, F., Mechie, J., Tilmann, F., 2016. Deep India meets deep Asia: Lithospheric indentation, delamination and break-off under Pamir and Hindu Kush (Central Asia). Earth Planet Sci Lett 435, 171–184. https://doi.org/10.1016/J.EPSL.2015.11.046

Lamb, S., 2015. Kinematics to dynamics in the New Zealand Plate boundary zone: implications for the strength of the lithosphere. Geophys J Int 201, 552–573. https://doi.org/10.1093/GJI/GGV027

Lin, S.C., Kuo, B.Y., 2016. Dynamics of the opposite-verging subduction zones in the Taiwan region: Insights from numerical models. J Geophys Res Solid Earth 121, 2174–2192. https://doi.org/10.1002/2015JB012784

Maiti, G., Roy, A., Sen, J., Mandal, N., 2021. Impact of Decelerating India-Asia Convergence on the Crustal Flow Kinematics in Tibet: An Insight From Scaled Laboratory Modeling. Geochemistry, Geophysics, Geosystems 22, e2021GC009967. https://doi.org/10.1029/2021GC009967

Mansour, J., Giordani, J., Moresi, L., Beucher, R., Kaluza, O., Velic, M., Farrington, R., Quenette, S., Beall, A., 2020. Underworld2: Python Geodynamics Modelling for Desktop, HPC and Cloud. J Open Source Softw 5, 1797. https://doi.org/10.21105/joss.01797

Maunder, B., Prytulak, J., Goes, S., Reagan, M., 2020. Rapid subduction initiation and magmatism in the Western Pacific driven by internal vertical forces. Nature Communications 2020 11:1 11, 1–8. https://doi.org/10.1038/s41467-020-15737-4

Merkouriev, S.A., Sotchevanova, N.A., 2003. Structure and evolution of the Carlsberg Ridge: Evidence for non-stationary spreading on old and modern spreading centres on JSTOR [WWW Document]. Curr Sci. URL https://www.jstor.org/stable/24108663 (accessed 11.8.23).

Miles, P.R., 1982. Gravity models of the Amirante Arc, western Indian Ocean. Earth Planet Sci Lett 61, 127–135. https://doi.org/10.1016/0012-821X(82)90045-0

Mishin, Y.A., Gerya, T. V., Burg, J.P., Connolly, J.A.D., 2008. Dynamics of double subduction: Numerical modeling. Physics of the Earth and Planetary Interiors 171, 280–295. https://doi.org/10.1016/J.PEPI.2008.06.012

Molnar, P., Stock, J.M., 2009. Slowing of India's convergence with Eurasia since 20 Ma and its implications for Tibetan mantle dynamics. Tectonics. https://doi.org/10.1029/2008TC002271

Peral, M., Király, Á., Zlotnik, S., Funiciello, F., Fernàndez, M., Faccenna, C., Vergés, J., 2018. Opposite Subduction Polarity in Adjacent Plate Segments. Tectonics 37, 3285–3302. https://doi.org/10.1029/2017TC004896

Peron-Pinvidic, G., Gernigon, L., Gaina, C., Ball, P., 2012. Insights from the Jan Mayen system in the Norwegian–Greenland sea—I. Mapping of a microcontinent. Geophys J Int 191, 385–412. https://doi.org/10.1111/J.1365-246X.2012.05639.X

Phukon, P., 2022. Nature of the northern Indian plate margin during the assembly of supercontinent Columbia: was it a part of a double subduction? Earth Sci Rev 233, 104185. https://doi.org/10.1016/J.EARSCIREV.2022.104185

Pusok, A.E., Stegman, D.R., 2020. The convergence history of India-Eurasia records multiple subduction dynamics processes. Sci Adv 6. https://doi.org/10.1126/SCIADV.AAZ8681/SUPPL_FILE/AAZ8681_SM.PDF

Pusok, A.E., Stegman, D.R., 2019. Formation and Stability of Same-Dip Double Subduction Systems. J Geophys Res Solid Earth 124, 7387–7412. https://doi.org/10.1029/2018JB017027

Sandiford, D., Moresi, L., 2019. Improving subduction interface implementation in dynamic numerical models. Solid Earth. https://doi.org/10.5194/se-10-969-2019

Sengupta, S., Ray, K.K., Acharyya, S.K., de Smeth, J.B., 1990. Nature of ophiolite occurrences along the eastern margin of the Indian plate and their tectonic significance. Geology 18, 439–442. https://doi.org/10.1130/0091-7613(1990)018<0439:NOOOAT>2.3.CO;2

Spiegelman, M., Katz, R.F., 2006. A semi-Lagrangian Crank-Nicolson algorithm for the numerical solution of advection-diffusion problems. Geochemistry, Geophysics, Geosystems 7. https://doi.org/10.1029/2005GC001073

Stern, R.J., 2004. Subduction initiation: spontaneous and induced. Earth Planet Sci Lett 226, 275–292. https://doi.org/10.1016/J.EPSL.2004.08.007

Stern, R.J., 2002. SUBDUCTION ZONES. Reviews of Geophysics 40, 3–1. https://doi.org/10.1029/2001RG000108

Stevens, D.E., McNeill, L.C., Henstock, T.J., Delescluse, M., Chamot-Rooke, N., Bull, J.M., 2020. A complete structural model and kinematic history for distributed deformation in the Wharton Basin. Earth Planet Sci Lett 538, 116218. https://doi.org/10.1016/J.EPSL.2020.116218

Tilling, R.I., 1996. Hazards and Climatic Impact of Subduction-Zone Volcanism: A Global and Historical Perspective. Geophysical Monograph Series 96, 331–335. https://doi.org/10.1029/GM096P0331

Van Der Voo, R., Spakman, W., Bijwaard, H., 1999. Tethyan subducted slabs under India. Earth Planet Sci Lett 171, 7–20. https://doi.org/10.1016/S0012-821X(99)00131-4

Van Hinsbergen, D.J.J., Kapp, Paul, Dupont-Nivet, Guillaume, Lippert, Peter C, Decelles, Peter G, Torsvik, Trond H, Hinsbergen, V., Kapp, P, Dupont-Nivet, G, Lippert, P C, Decelles, P G, Torsvik, T H, 2011. Restoration of Cenozoic deformation in Asia and the size of Greater India. Tectonics 30, 5003. https://doi.org/10.1029/2011TC002908

van Hunen, J., Allen, M.B., 2011. Continental collision and slab break-off: A comparison of 3-D numerical models with observations. Earth Planet Sci Lett 302, 27–37. https://doi.org/10.1016/j.epsl.2010.11.035

Vignaroli, G., Faccenna, C., Jolivet, L., Piromallo, C., Rossetti, F., 2008. Subduction polarity reversal at the junction between the Western Alps and the Northern Apennines, Italy. Tectonophysics 450, 34–50. https://doi.org/10.1016/J.TECTO.2007.12.012

Westerweel, J., Roperch, P., Licht, A., Dupont-Nivet, G., Win, Z., Poblete, F., Ruffet, G., Swe, H.H., Thi, M.K., Aung, D.W., 2019. Burma Terrane part of the Trans-Tethyan arc during collision with India according to palaeomagnetic data. Nature Geoscience 2019 12:10 12, 863–868. https://doi.org/10.1038/s41561-019-0443-2

Yin, A., Harrison, T.M., 2000. Geologic Evolution of the Himalayan-Tibetan Orogen. https://doi.org/10.1146/annurev.earth.28.1.211 28, 211–280. https://doi.org/10.1146/ANNUREV.EARTH.28.1.211

Zhang, Q., Guo, F., Zhao, L., Wu, Y., 2017. Geodynamics of divergent double subduction: 3-D numerical modeling of a Cenozoic example in the Molucca Sea region, Indonesia. J Geophys Res Solid Earth 122, 3977–3998. https://doi.org/10.1002/2017JB013991

Zhou, X., Li, Z.H., Gerya, T. V., Stern, R.J., Xu, Z., Zhang, J., 2018. Subduction initiation dynamics along a transform fault control trench curvature and ophiolite ages. Geology 46, 607–610. https://doi.org/10.1130/G40154.1

Zhu, M., Yan, Z., Pastor-Galán, D., Chen, L., Miao, L., Zhang, F., Li, S., Yang, S., 2023. Do microcontinents nucleate subduction initiation? Geology 51, 668–672. https://doi.org/10.1130/G51222.1/5849054/G51222.PDF

Supplementary information for:

Dynamic evolution of competing same-dip double subduction: New perspectives of the Neo-Tethyan plate tectonics

Arnab Roy[1], Nibir Mandal[1], Jeroen Van Hunen[2]

[1]High Pressure and Temperature Laboratory, Department of Geological Sciences, Jadavpur University, Kolkata 700032, India.
[2]Department of Earth Sciences, Durham University, Durham, UK

S1. Strain-Rate Mapping

We quantify the strain rate field with the square root of the second invariant of the deviatoric strain rate tensor, $\dot{\varepsilon}_{ij}$ for the three different dynamic double subduction models presented in the main text (Figs 3,4,5). High values of $\dot{\varepsilon}_{ij}$ indicate regions of intense deformation whereas low

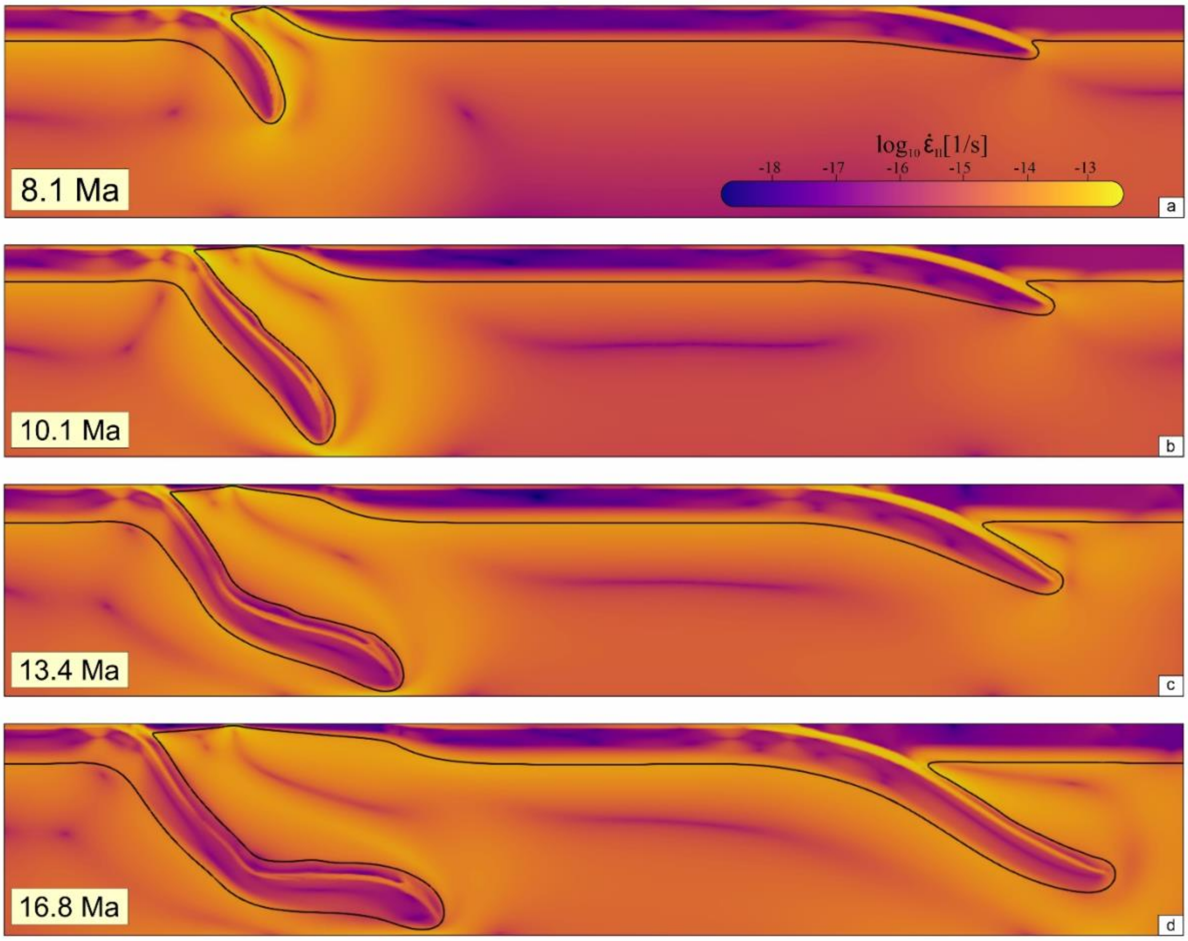

Figure S1. Second strain rate invariant evolution for double subduction model in an oceanic setting, (a–d), for same configuration as Figs 3(a)–(e). Black lines show the thermally controlled Lithosphere Asthenosphere Boundary (LAB) plotted as an isotherm.

values indicate regions of little deformation. The distribution and magnitude of $\dot{\varepsilon}_{ij}$, hence, indicates, for example, whether the deformation around a subduction system and within the slab is either more or less homogeneous or strongly heterogeneous. In this section, we present the strain-rate plots of the three double subduction models presented in the main text: a) oceanic plate model (Fig. S1), b) microcontinent-ocean model (Fig. S2), and c) multiple continent model (Fig. S3).

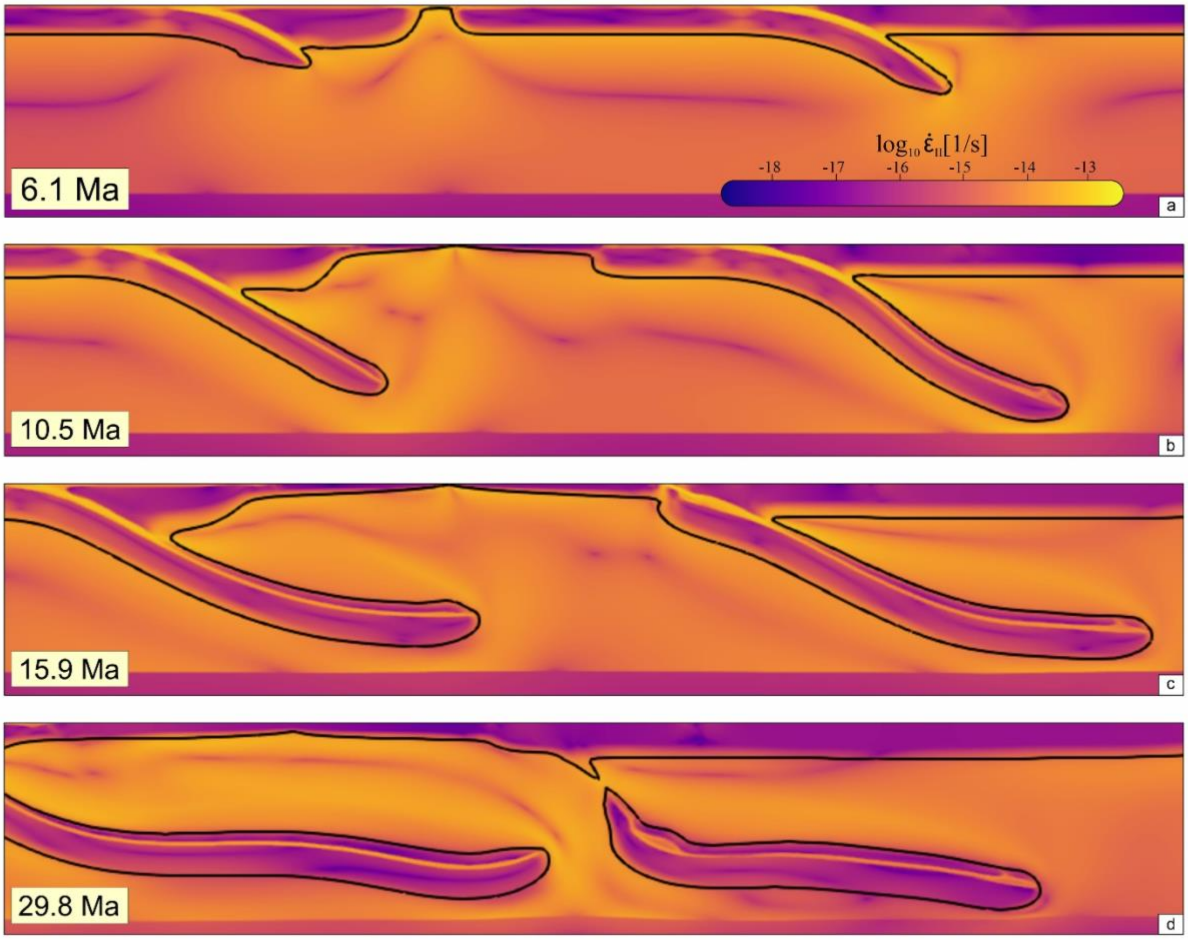

Figure S2. Second strain rate invariant evolution for double subduction model in an ocean-continent setting, (a–d), for same configuration as Figs 4(a)–(e). Black lines show the thermally controlled LAB plotted as an isotherm.

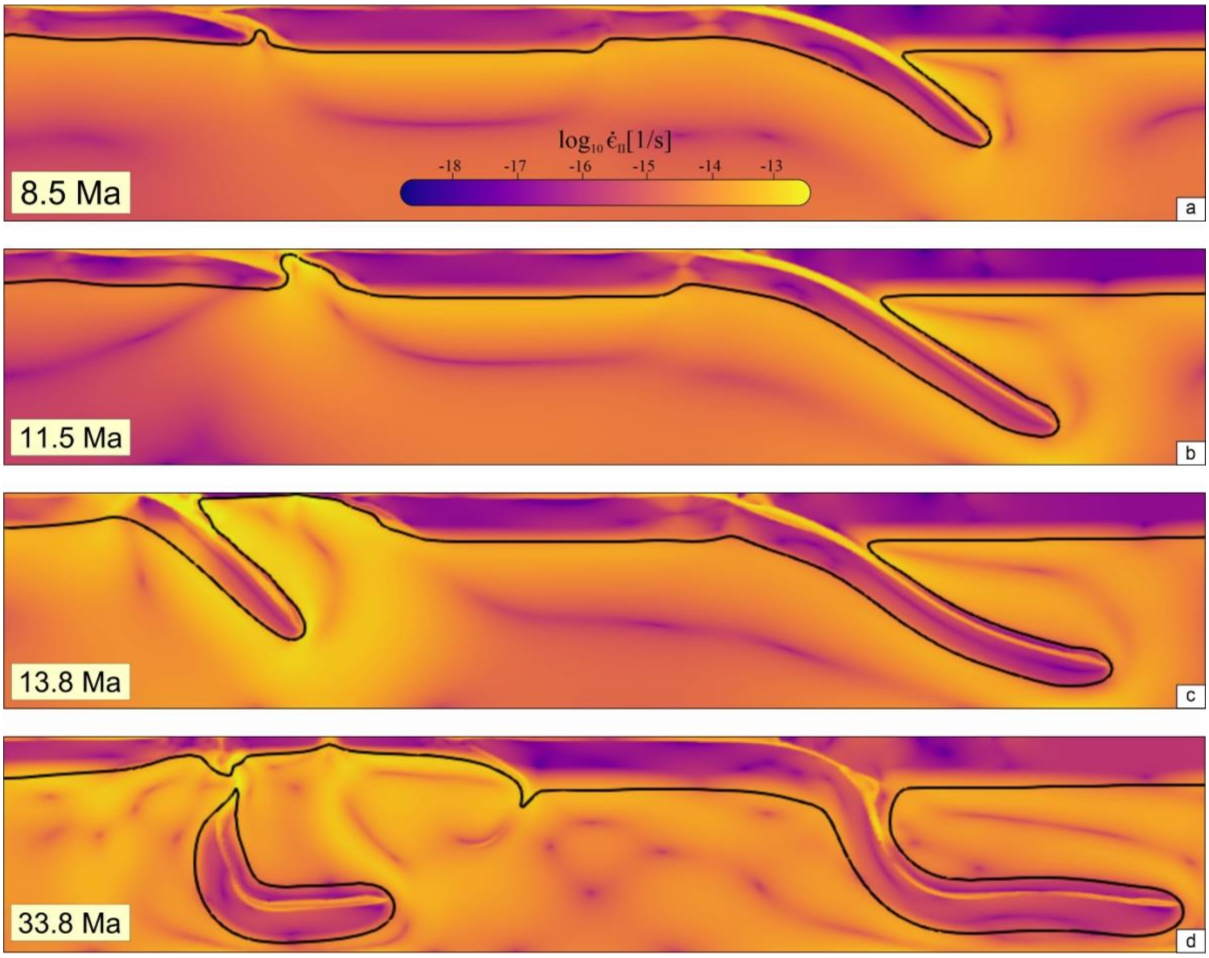

Figure S3. Second strain rate invariant evolution for double subduction model in presence of continent-continent collision, (a–d), for same configuration as Figs 5(a)–(e). Black lines show the thermally controlled LAB plotted as an isotherm.

S2. Mesh Resolution Tests

Rigorous mesh resolution tests are required to study the resolution dependency of visco-plastic models before applying them in interpreting the natural phenomenon under consideration. In the resolution test we set a base vertical resolution of 128 and a mesh aspect ratio of 2.25:1, and progressively increase the mesh resolutions as 576 x 256, 1150 x 512 and 2300 x 1024 to evaluate their effects on the model results. The resolution was optimized to a value (1150 x 512) when the model outputs, e.g., calculated trench velocity (V_T) did not change significantly (Fig. S4) with further increasing resolution level. Under this optimized mesh resolution and refinement the model yielded low shear stresses (~12Mpa) at the subduction interface during the initiation of each single-sided subduction.

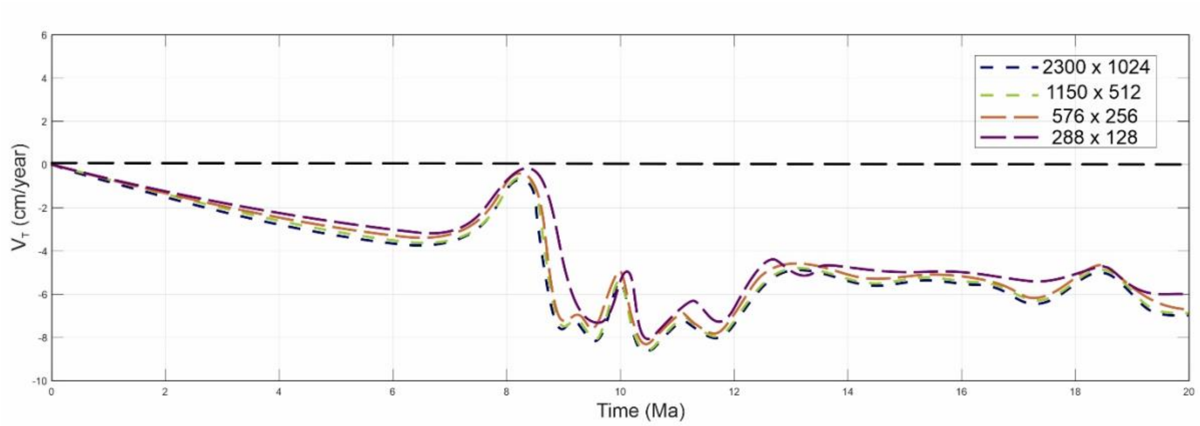

Figure S4: Mesh resolution tests using the trench velocity (V_T) as a function of time at the rear subduction zone of the oceanic double subduction model. Four different resolutions are shown in the legend.